J. Fluid Mech. (2015), *vol.* 772, *pp.* 445–477. © Cambridge University Press 2015
doi:10.1017/jfm.2015.203

Effect of a mesh on boundary layer transitions induced by free-stream turbulence and an isolated roughness element

P. Phani Kumar[1], A. C. Mandal[2] and J. Dey[1,†]

[1]Department of Aerospace Engineering, Indian Institute of Science, Bangalore 560012, India

[2]Department of Aerospace Engineering, Indian Institute of Technology, Kanpur, UP 208016, India

(Received 21 September 2014; revised 22 February 2015; accepted 27 March 2015;
first published online 7 May 2015)

Streamwise streaks, their lift-up and streak instability are integral to the bypass transition process. An experimental study has been carried out to find the effect of a mesh placed normal to the flow and at different wall-normal locations in the late stages of two transitional flows induced by free-stream turbulence (FST) and an isolated roughness element. The mesh causes an approximately 30 % reduction in the free-stream velocity, and mild acceleration, irrespective of its wall-normal location. Interestingly, when located near the wall, the mesh suppresses several transitional events leading to transition delay over a large downstream distance. The transition delay is found to be mainly caused by suppression of the lift-up of the high-shear layer and its distortion, along with modification of the spanwise streaky structure to an orderly one. However, with the mesh well away from the wall, the lifted-up shear layer remains largely unaffected, and the downstream boundary layer velocity profile develops an overshoot which is found to follow a plane mixing layer type profile up to the free stream. Reynolds stresses, and the size and strength of vortices increase in this mixing layer region. This high-intensity disturbance can possibly enhance transition of the accelerated flow far downstream, although a reduction in streamwise turbulence intensity occurs over a short distance downstream of the mesh. However, the shape of the large-scale streamwise structure in the wall-normal plane is found to be more or less the same as that without the mesh.

Key words: boundary layer control, boundary layers, transition to turbulence

1. Introduction

Otherwise stable laminar flows are known to undergo transition in the presence of high free-stream turbulence (FST), surface roughness, etc. Although the route to transition differs, low- and high-speed streamwise streaks are seen in many transitional flows. In transition induced by a high level of FST, only low-frequency components of the FST penetrate the boundary layer, mainly near the leading edge (e.g. Kendall 1998; Schrader *et al.* 2010), resulting in the formation of streaks due to the lift-up effect (Landahl 1980). A low-speed streak is associated with an inclined high-shear

†Email address for correspondence: jd@aero.iisc.ernet.in

layer, and its instability is mainly responsible for flow breakdown; in contrast to this, a high-speed streak is confined close to the wall (e.g. Jacobs & Durbin 2001; Mandal, Venkatakrishnan & Dey 2010; Nolan & Zaki 2013). Although the low-frequency component of the FST plays an important role in bypass transition, the high-frequency component may be relevant in streak breakdown (Zaki & Durbin 2005). The complex process of FST-induced transition has been reviewed by many investigators in the past (e.g. Durbin & Wu 2007; Schlatter *et al.* 2008; Zaki 2013); the recent review by Brandt (2014) elucidates various important aspects of the lift-up process and the resulting non-modal growth of streaks in wall-bounded shear flows.

Jacobs & Durbin (2001) and Zaki & Durbin (2005) suggest that breakdown in FST-induced transition occurs at the boundary layer edge due to a Kelvin–Helmholtz type instability between a lifted-up inclined shear layer having negative streamwise velocity fluctuations and free-stream eddies. Brandt & de Lange (2008) suggest that, even in the absence of free-stream disturbances, breakdown can also occur at the interface of low- and high-speed streaks inside the boundary layer. Nolan & Walsh (2012) also suggest a similar breakdown scenario from their experimental study of transition due to FST. Although flow breakdown can occur in the outer region or inside the boundary layer, Hack & Zaki (2014) suggest that breakdown in a Blasius boundary layer mainly occurs through instabilities in the outer region. It is also known that streamwise streaks exhibit sinuous and varicose type oscillations during the breakdown process in FST-induced transition (e.g. Matsubara & Alfredsson 2001; Brandt, Schlatter & Henningson 2004; Mans *et al.* 2005; Ovchinnikov, Choudhari & Piomelli 2008). Concerning the turbulent spot precursor, a staggered pattern of quasi-streamwise vortices is seen along the flanks of a low-speed streak in sinuous type breakdown (e.g. Brandt *et al.* 2004; Mans *et al.* 2005; Schlatter *et al.* 2008; Mandal *et al.* 2010), whereas hairpin- or Λ-like structures are seen in varicose type breakdown (e.g. Brandt *et al.* 2004; Mans *et al.* 2005). In terms of the streamwise velocity fluctuations, Hernon, Walsh & McEligot (2007) suggest that, at the onset of transition, the intensities of the peak negative and positive fluctuations are approximately 40 % and 30 % of the free-stream velocity respectively. Further, they find that the peak positive and negative fluctuation intensities occur close to the wall and near the boundary layer edge respectively, as also reported by Mandal *et al.* (2010) by separating these quantities from their measured data; their values exceed 25 % of the free-stream velocity. Nolan & Zaki (2013), who applied streak detection and laminar–turbulent discrimination algorithms, suggest that only streaks of amplitude greater than 20 % of the local free-stream velocity break down to turbulence.

Apart from FST, suction or blowing at the wall (e.g. Elofsson, Kawakami & Alfredsson 1999), free-stream vortex (e.g. Bertolotti & Kendall 1997; Boiko 2001) and roughness elements (e.g. Bakchinov *et al.* 1995; White 2002; Fransson *et al.* 2004) also generate streaks in boundary layers. Such artificial streaks have often been used to study the breakdown characteristics in a somewhat controlled manner (e.g. Asai, Minagawa & Nishioka 2002; Litvinenko *et al.* 2005; Brandt 2007; Wang, Pan & Zhang 2009). For instance, Asai *et al.* (2002) have studied instability and breakdown of a near-wall low-speed streak, generated by a small screen placed on the wall. Transition due to a single roughness element (e.g. Tani *et al.* 1962; Acarlar & Smith 1987; Klebanoff, Cleveland & Tidstrom 1992) or due to an array of roughness elements (e.g. Bakchinov *et al.* 1995; Zhang, Pan & Wang 2011) has been investigated in the past. In the case of a single roughness element of hemispherical shape, the element is wrapped by a vortex and vortices are shed from the roughness

element itself (e.g. Acarlar & Smith 1987; Klebanoff *et al.* 1992). The simulation of transition induced by an array of roughness elements by Choudhari & Fischer (2005) shows that a high-shear layer that extends from the tip of the roughness element begins to shed vortices downstream. Similar vortex shedding from a high-shear layer is also seen in the case of transition caused by a vortex generator that spans half the flat plate (Manu 2013).

Streamwise streaks and their lift-up, vortex shedding from the high-shear layer, etc. are normally seen in transitional flows. Therefore, if the lift-up of the high-shear layer or vortex shedding from it is disturbed by some external means, then the downstream flow will change. With this in mind, a mesh was placed normal to the flow and at different wall-normal locations in the late stage of transition to study the effect of acceleration and reduced free-stream velocity caused by it (e.g. Bi *et al.* 2014) on transitional flows induced by (i) an isolated cylindrical roughness element and (ii) FST; the second case has been studied in detail. In a different context, the use of a screen is known to alter flow downstream of a circular cylinder (Oruç 2012). It was found that a mesh placed close to the wall caused transition delay over a large distance, which should be viewed as an important aspect of transition manipulation rather than a transition control strategy. In the case of a mesh away from the wall, disturbances generated by it in the outer boundary layer region possibly cause a faster transition of the mildly accelerated flow.

In the context of transition delay, a brief review of past transition control strategies seems relevant here, as any control may modify, even if mildly, the flow downstream. Control of near-wall events in transitional flows has been studied by many researchers in the past. For example, Lundell & Alfredsson (2003) and Lundell (2007) used localized suction to delay transition of steady and time-varying streaks generated by suction in a plane channel flow and randomly induced streaks by FST in a boundary layer. While the transition delay in the channel flow was attributed to the reduced spanwise gradient of the streamwise velocity causing a slower growth of secondary disturbances introduced into the flow, FST-induced transition was delayed due to reduced energy of low-frequency fluctuations near the wall. Monokrousos *et al.* (2008) have also reported a delay in FST-induced transition by linear feedback control with suction and blowing at the wall. Further, they suggest that as the outer region of the boundary layer is less affected by such controls, recovery of streaks occurs rapidly downstream. Hanson *et al.* (2014) have used plasma actuators to control the transient growth of streaks generated in a laminar boundary layer by a spanwise array of roughness elements; the plasma actuators in their study generated streaks of spanwise phase opposite to those generated by the roughness array. Use of optimal streaks to stabilize the Tollmien–Schlichting wave was reported by Cossu & Brandt (2002) and verified by Fransson *et al.* (2005, 2006). Finite-amplitude stable streaks generated by a spanwise array of miniature vortex generators have also been used (Shahinfar *et al.* 2013; Shahinfar, Sattarzadeh & Fransson 2014) to delay transitions due to the Tollmien–Schlichting wave, a single oblique wave and a pair of oblique waves. However, the introduction of such stable streaks in a boundary layer subjected to a high level of FST resulted in early transition (Schlatter *et al.* 2010).

This paper is organized as follows. The experimental details and data processing technique adopted here are described in § 2. The results are presented and discussed in § 3, followed by a summary in § 4.

2. Experimental details and data processing

The present experimental study was carried out in the facility used in our previous studies (Mandal *et al.* 2010; Manu, Mathew & Dey 2010; Mandal & Dey 2011).

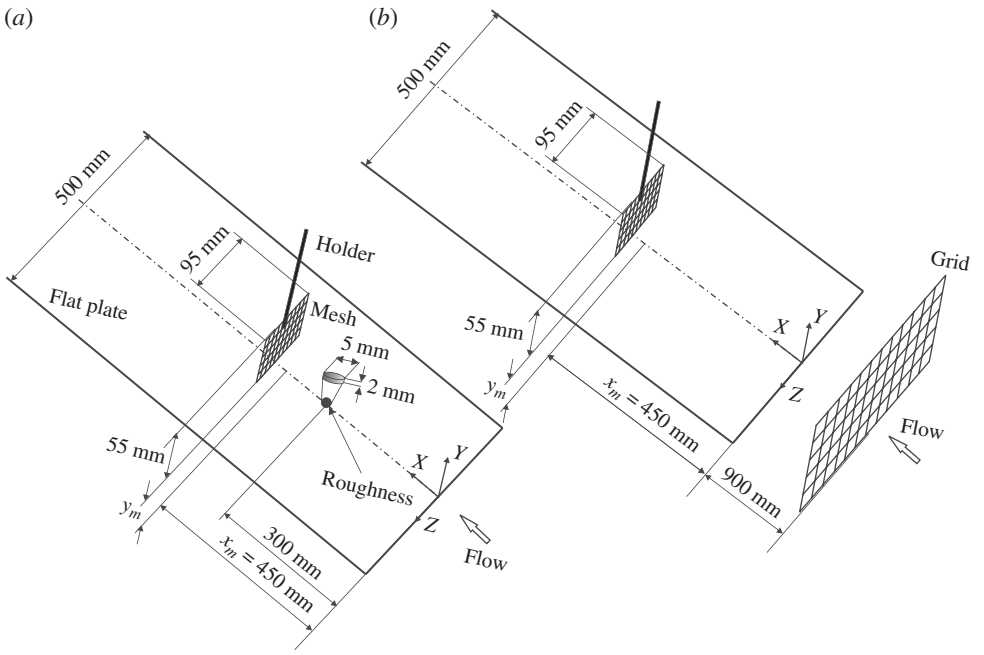

FIGURE 1. Schematic of the set-up showing the location of (*a*) the roughness element and the mesh in roughness-induced transition and (*b*) the grid and the mesh in FST-induced transition.

Briefly, the measurements were made on a flat plate placed in the mid-plane of the test section (500 mm × 500 mm × 3000 mm) of a low-turbulence wind tunnel. The leading edge of the plate was of semi-elliptical shape (Narasimha & Prasad 1994), and the FST, based on the streamwise velocity fluctuation, was 0.07 % at 20 m s^{-1}. The streamwise variation of the pressure coefficient, C_p, in the free stream was found to be within ±1 % in the region 150 mm $\leqslant x \leqslant$ 1000 mm; x is the streamwise distance from the leading edge.

As shown in figure 1(*a*), a single roughness element of 5 mm diameter (d) and 2 mm height (h) was placed at $x = 300$ mm from the leading edge of the plate; y and z denote the wall-normal and spanwise distances respectively. The roughness element was of hard rubber. The free-stream velocity in roughness-induced transition was $U_\infty = 5.3$ m s^{-1}. The dimensions of the roughness element used are comparable to those used by Bade & Naguib (2012).

The FST-induced transition was initiated by a grid made of cylindrical rods of diameter 8 mm with a spacing of 55 mm between them. A schematic of the experimental set-up showing the location of the grid is shown in figure 1(*b*). The free-stream velocity was $U_\infty = 3$ m s^{-1} and the FST intensity at the leading edge was 3 %. The FST generated was nearly isotropic in the measurement region (as observed in our unpublished data, details of which will be reported elsewhere). Without the roughness element or grid, a Blasius boundary layer was established over the plate.

Two stainless steel woven wire meshes of width × height = 21 mm × 55 mm (hereafter, SM) and 95 mm × 55 mm (hereafter, LM) were used. The mesh, held from a height gauge on the tunnel roof by a small rod (of diameter 4 mm), was placed at a downstream distance of $x_m = 450$ mm from the leading edge (figure 1)

and at different locations, y_m, from the wall. The dimensions of the mesh used were wire diameter = 0.28 mm, mesh size = 1.88 mm × 1.81 mm and porosity ≈72 %. The reason for placing the mesh at $x_m = 450$ mm is given in the following. In the case of SM, far downstream flow was affected by disturbances generated by its side edges. In order to avoid this, LM was mostly used.

The particle image velocimetry (PIV) unit (IDTpiv, USA) consisted of a double-cavity Nd:YAG laser (New Wave Research), laser sheet optics, a charge-coupled device (CCD) camera (1360 pixel × 1036 pixel) and the associated data processing software (proVISION ⅄). The CCD camera with 50 mm focal length lens could capture five image pairs per second. The interrogation window was of 24 pixel × 24 pixel, and the measurement resolution in terms of the correlation window size was approximately 1 mm; further details of data processing are reported in Mandal *et al.* (2010). The flow was seeded by smoke from a commercial fog generator. The PIV measurement region is denoted by $\Delta x \times \Delta y$ in the x–y plane and $\Delta x \times \Delta z$ in the x–z plane; $\Delta x \times \Delta z \approx 57$ mm × 45 mm and $\Delta x \times \Delta y \approx 50$ mm × 40 mm were used. The mean quantities were obtained by averaging 450–500 PIV image pairs at each measurement location; in FST-induced transition, a higher number of image pairs was also used, as deemed necessary.

The flow was monitored by a constant-temperature hot-wire anemometer placed at $x = 750$ mm from the leading edge of the plate and in the mid-plane ($z = 0$).

The instantaneous streamwise velocity, U_I, is $U_I = U + u$, where U is the mean velocity and u is the fluctuating component; similarly, for the wall-normal and spanwise components, $V_I = V + v$ and $W_I = W + w$ respectively. All wall-normal PIV measurements were made along the plate centreline ($z = 0$), unless specified otherwise.

The two-point spatial correlation for any two quantities, A and B, in the x–y or x–z plane (Hong, Katz & Schultz 2011; Rahgozar & Maciel 2012), is

$$R_{AB}(x_r + \delta x, y_r + \delta y) = \frac{\overline{A(x_r, y_r)B(x_r + \delta x, y_r + \delta y)}}{\sigma_A(x_r, y_r)\sigma_B(x_r + \delta x, y_r + \delta y)}, \tag{2.1}$$

$$R_{AB}(x_r + \delta x, z_r + \delta z) = \frac{\overline{A(x_r, z_r)B(x_r + \delta x, z_r + \delta z)}}{\sigma_A(x_r, z_r)\sigma_B(x_r + \delta x, z_r + \delta z)}, \tag{2.2}$$

where the subscript r denotes the reference location and σ is the root-mean-square of a given quantity; δx, δy and δz denote the separation distances from the respective reference location. Auto- and cross-correlations of velocity fluctuations, and the swirl strength, λ, were considered.

Vortices were identified following Adrian, Christensen & Liu (2000) for 2D PIV data; λ is the imaginary part of the complex eigenvalue of the local velocity gradient tensor. For swirl correlations and vortex statistics, only vortices of size greater than or equal to the PIV interrogation size were retained, without applying any threshold on the magnitude of the swirl strength. Although $\lambda \geqslant 0$ by definition, a sign based on the local vorticity is assigned to it to distinguish clockwise ($\lambda < 0$) and anticlockwise ($\lambda > 0$) vortices (Wu & Christensen 2006).

3. Results and discussion

3.1. *Effect of a mesh on roughness-induced transition*

Without the roughness element, the measured Blasius boundary layer thickness and the displacement thickness at $x = 300$ mm were $\delta_B = 5.45$ mm and $\delta_B^* = 1.9$ mm

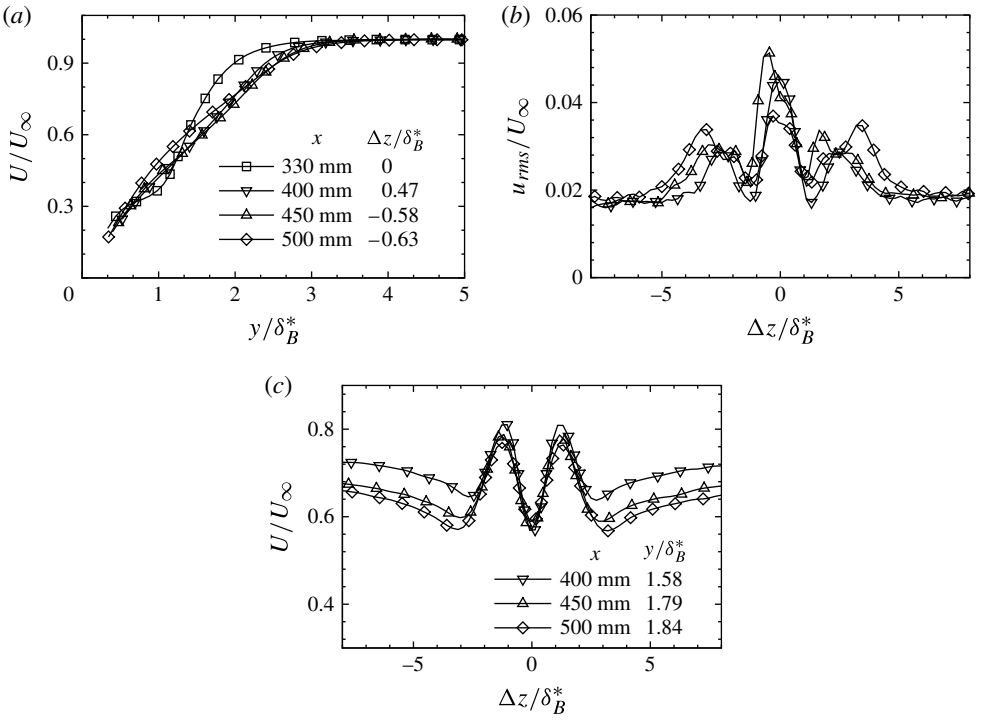

FIGURE 2. Streamwise velocity and intensity of fluctuations due to roughness. (*a*) Boundary layer velocity profiles; (*b*) spanwise variation of the fluctuation intensity; (*c*) spanwise variation of the streamwise velocity. The values of $\Delta z/\delta_B^*$ in (*a*) and y/δ_B^* in (*c*) indicate spanwise and wall-normal PIV measurement locations respectively.

respectively, for a free-stream velocity of $U_\infty = 5.3$ m s^{-1}. The roughness height (of 2 mm) was approximately equal to δ_B^*; that is, the roughness element was within the boundary layer. The Reynolds number based on the roughness height was Re_h $(= U_h h/\nu) = 396$; U_h is the mean velocity at a height h without the roughness element and ν is the kinematic viscosity; this value is higher than the critical value of $Re_h = 338$ suggested by Bade & Naguib (2012) for a single roughness element. Most of the flow parameters are normalized with U_∞ $(= 5.3$ m s$^{-1})$ and δ_B^* in the following.

Downstream of the roughness element, the boundary layer velocity profiles at different streamwise locations are shown in figure 2(*a*). The flow just behind the roughness element underwent separation and the bubble extended until approximately $x = 310$ mm. The spanwise variation of u_{rms}, the root-mean-square of the streamwise fluctuating velocity component u due to the roughness element alone showed prominent peaks at $\Delta z/\delta_B^* \approx 0, \pm 3$, as can be seen in figure 2(*b*). This indicates the presence of low- and high-speed streaks, as can also be seen in the spanwise variation of U/U_∞ in figure 2(*c*). As u_{rms} variation is significant within $\Delta z/\delta_B^* = \pm 5$ until approximately $x = 500$ mm, SM (of 21 mm width) was initially considered. Due to the finite mesh width, flow in the mid-plane was slightly contaminated by disturbances generated along its sides. Therefore, to avoid this, LM (which is wider than SM) was mostly used.

The instantaneous PIV measurements in the wall-normal and spanwise planes in figure 3 show a typical flow picture at $x = 450$ mm due to the roughness element;

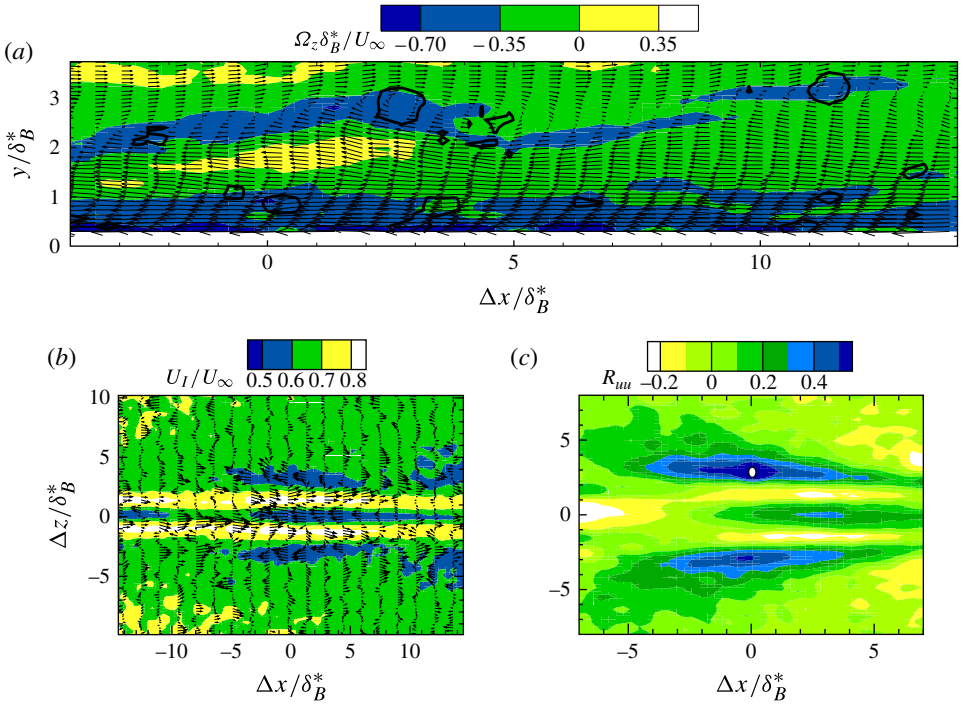

FIGURE 3. (Colour online) (*a*) Instantaneous spanwise vorticity contours in the wall-normal plane at $x = 450$ mm illustrating the inclined high-shear layer in roughness-induced (R) transitional flow. The arrows are fluctuating velocity vectors of u and v seen by an observer moving at a convection velocity of $0.85U_\infty$. The line contours represent the swirl strength. (*b*) Instantaneous streamwise velocity contours in the spanwise plane showing the varicose instability feature. The arrows are fluctuating velocity vectors of u and w. (*c*) Correlation contours of the streamwise velocity fluctuation (R_{uu}); the white dot indicates the reference location. The wall-normal plane is at $\Delta z/\delta_B^* \approx -0.58$ and the spanwise plane is at $y/\delta_B^* \approx 1.79$.

here (and in the following), R denotes the roughness-alone case. We may note that the camera centre here (and hereafter) is at $\Delta x = 0$. Figure 3(*a*) shows high-shear layers with detached vortices extending well into the free stream in the wall-normal plane. The colour contours in this figure correspond to the normalized spanwise vorticity, $\Omega_z\delta_B^*/U_\infty$; Ω_z is the dimensional spanwise vorticity. The line contours correspond to vortices, and the superimposed vectors are those seen by an observer moving with a convection velocity (U_C) of 0.85 U_∞. The breakdown of flow shown in figure 3(*b*) is similar to that observed by Chernoray *et al.* (2006) in varicose instability (see their figure 6) triggered by artificial disturbances introduced on streaks generated by a single roughness element. Bade & Naguib (2012) have also observed similar breakdown in their flow visualization. The contours in this figure correspond to the non-dimensional instantaneous velocity (U_I/U_∞), and the superimposed vectors are fluctuating velocities. In terms of the correlation contours of the streamwise velocity fluctuation, R_{uu}, the breakdown pattern is shown in figure 3(*c*). The choice of a mesh at $x_m = 450$ mm was based on the fact that it would prevent the lift-up of the inclined high-shear layer seen in figure 3(*a*) and also distort the symmetric streaky structure (figure 3*b*).

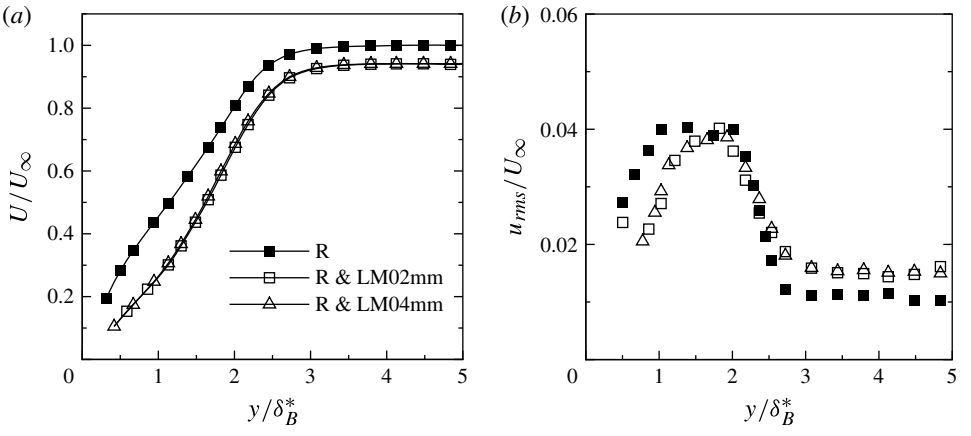

FIGURE 4. Effect of a mesh on the upstream flow. Boundary layer velocity (*a*) and fluctuation intensity (*b*) profiles at $x = 400$ mm and $\Delta z/\delta_B^* \approx 0.47$.

Upstream of the mesh, the free-stream velocity at $x = 400$ mm is slightly lower than the roughness-alone case due to the blockage caused by it, as shown in figure 4(*a*); note that the velocity is normalized by $U_\infty = 5.3$ m s^{-1} (of the roughness-alone case) to show this effect; here (and in the following), R & LM02mm, R & LM04mm, etc., indicate that the large mesh was placed at $y_m = 2$ mm, 4 mm, etc., in roughness-induced transitional flow. Further upstream, this reduction in free-stream velocity was less pronounced (not shown here). However, the u_{rms} profiles in figure 4(*b*) indicate that the peak fluctuation intensity is not so significantly altered upstream of the mesh.

The instantaneous velocity fields in the spanwise plane at $x = 500$ mm in figure 5 show the effect of LM at different y_m locations. The streak instability in the roughness-alone case can be clearly seen in figure 5(*a*). The instantaneous velocity field is symmetric along the centreline. The counter-rotating vortices (indicated by black and white lines) at the interface of low- and high-speed streaks (i.e. region of large shear) correspond to the legs of a hairpin vortex (e.g. Chernoray *et al.* 2006; Zhang *et al.* 2011). The streamwise (L) and spanwise (W) length scales of the instability determined following Mans *et al.* (2005) are also shown in figure 5(*a*). In FST-induced transition, Mans *et al.* (2005) find $L = 28\delta_0^*$ and $W = 2.5\delta_0^*$ for sinuous instability, and $L = 19\delta_0^*$ and $W = 5.5\delta_0^*$ for varicose instability; δ_0^* corresponds to $Re_{\delta_0^*} = 300$. As shown in figure 5(*a*), the values of $L = 38.2\delta_0^*$ and $W = 12.58\delta_0^*$ are almost twice those reported for the varicose instability in FST-induced transition. On introducing the mesh at $y_m = 2$ mm (figure 5*b*), the symmetric streaky structure associated with the instability (including vortices) is completely distorted. The mesh is seen to cause a large number of streaks of smaller spanwise spacing, an increase in instantaneous velocity and a reduction in velocity fluctuations. The velocity fluctuation across streaks is also very small. Vortices are still present, but are not as regular as in figure 5(*a*). By applying travelling waves with a certain phase shift in the spanwise plane, Bai *et al.* (2014) control the spanwise modulation of streaks to reduce drag in a turbulent boundary layer. The resulting orderly streaky structure is attributed to the frictional-drag reduction. Interestingly, their orderly streaky pattern (see their figure 10*b*) is qualitatively similar to that in figure 5(*b*). Thus, one may anticipate that the mesh at $y_m = 2$ mm will reduce the frictional drag, compared with the roughness-alone case, if orderly streaks are responsible for any such reduction. With

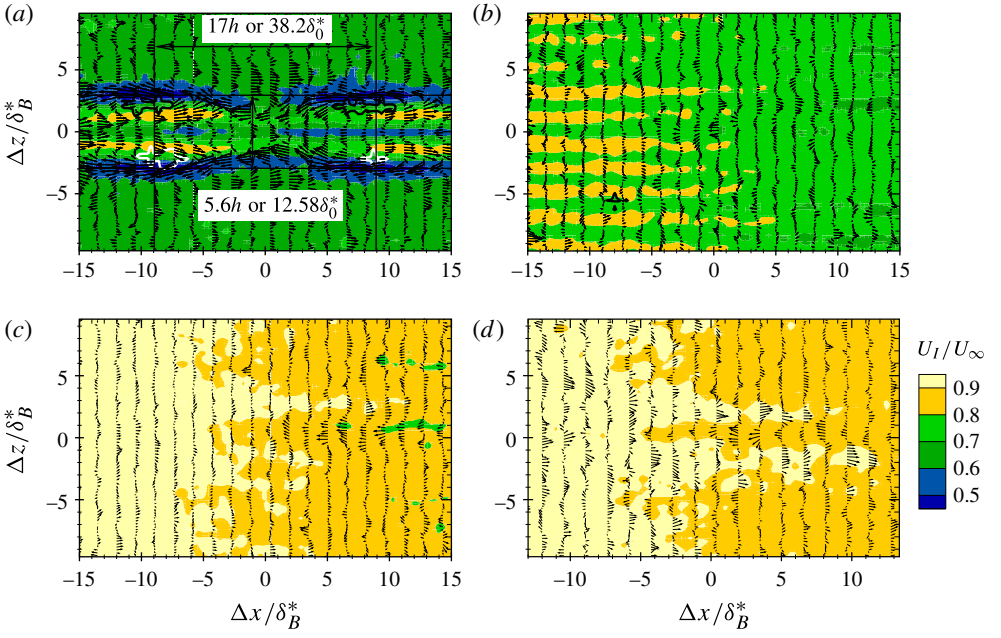

FIGURE 5. (Colour online) Instantaneous streamwise velocity contours in the spanwise plane at $x = 500$ mm showing the effect of a mesh at different wall-normal locations on roughness-induced transitional flow: (*a*) R; (*b*) R & LM02mm; (*c*) R & LM04mm; (*d*) R & LM06mm. The arrows are the fluctuating velocity vectors of u and w. The line contours represent the swirl strength (black line, anticlockwise vortex; white line, clockwise vortex). The spanwise plane is at $y/\delta_B^* \approx 1.84$ and h is the roughness height.

the mesh further away from the wall, the instantaneous velocity increases (figures 5*c*,*d*); the faint appearance of a low-speed streak in the centre can also be observed. Almost all of the instantaneous velocity fields (with mesh) were similar to those shown here. The spanwise variation of U at $x = 500$ mm in figure 6(*a*) shows that the mesh increases the acceleration and reduces the streak amplitude, $(U_{max} - U_{min})$ (Elofsson *et al.* 1999), thus reducing the spanwise gradient of the streamwise velocity; U_{max} and U_{min} are the maximum and minimum of the mean streamwise velocity in the spanwise plane respectively. While a significant reduction in u_{rms} is caused by the mesh (figure 6*b*), the greatest reduction is for the mesh at $y_m = 2$ mm.

The effect of a mesh on the boundary layer velocity profile at $x = 750$ mm is shown in figure 7(*a*). Compared with the roughness-alone case, the mesh reduces the free-stream velocity from 5.3 to 3.7 m s^{-1}, i.e. a reduction of approximately 30 %. This reduction is due to the pressure drop caused by the mesh. Nearly the same velocity profiles for both the SM and LM cases indicate that the flow history is less significant far downstream; this could be due to the fact that SM and LM differ only in width. Figure 7(*b*) shows that, compared with the roughness-induced transitional case (filled symbols), both SM and LM reduce u_{rms} considerably; the higher values across the boundary layer for SM are due to the contamination by disturbances from its sides, as mentioned earlier. This significant reduction of u_{rms} indicates transition delay caused by the mesh at $y_m = 2$ mm. A reduced free-stream velocity implies a lower mean flow Reynolds number ($Re = U_{fs}\theta/\nu$); U_{fs} is the local free-stream velocity and θ is the momentum thickness. Moreover, due to the transition delay, the boundary

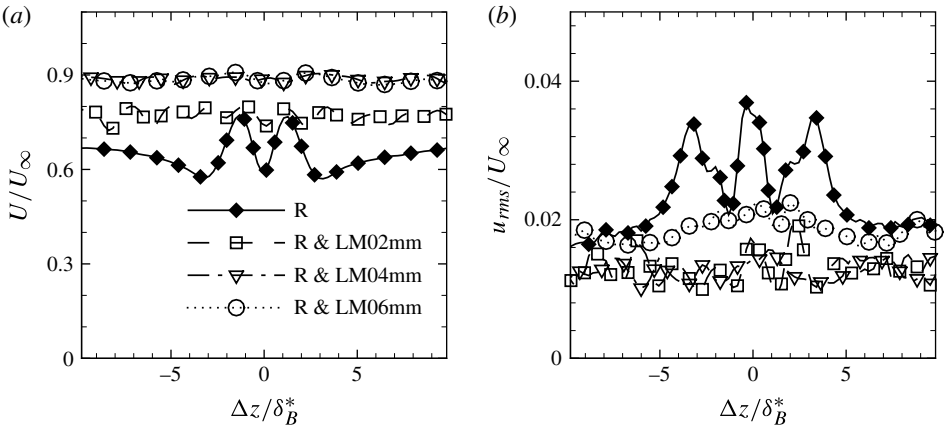

FIGURE 6. Comparison of the spanwise distribution of the streamwise mean velocity (*a*) and the fluctuation intensity (*b*) at $x = 500$ mm and $y/\delta_B^* \approx 1.84$ with and without the mesh.

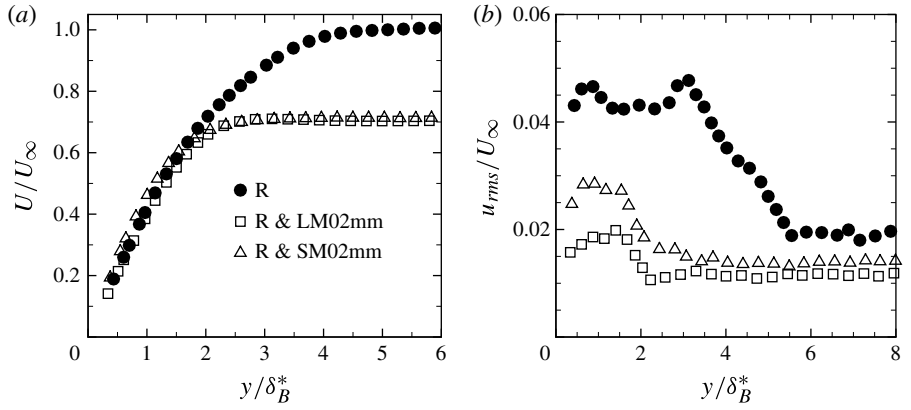

FIGURE 7. Effect of a mesh on the roughness-induced transitional flow. Boundary layer velocity (*a*) and fluctuation intensity (*b*) profiles at $x = 750$ mm and $\Delta z/\delta_B^* \approx 0.58$.

layer integral parameters at $x = 750$ mm are reduced, as shown in figure 8; δ^* and θ are based on U_{fs}; $\delta^* = \int_0^\infty [1 - (U/U_{fs})]\,\mathrm{d}y$ and $\theta = \int_0^\infty (U/U_{fs})[1 - (U/U_{fs})]\,\mathrm{d}y$.

The Reynolds number reduction seen here is similar to that in the relaminarization of a fully turbulent flow by a strong streamwise favourable pressure gradient (e.g. Blackwelder & Kovasznay 1972; Narasimha & Sreenivasan 1973; Piomelli, Balaras & Pascarelli 2000), where the boundary layer integral length scales also reduce. The transition delay reported here can be regarded as near relaminarization of the transitional flow. While an imposed favourable pressure gradient does not alter the shape of the large-scale spanwise structure in the relaminarization of fully turbulent flows (Blackwelder & Kovasznay 1972), a mesh here breaks down many transitional structures, as shown by the instantaneous PIV measurements in the wall-normal and spanwise planes at $x = 750$ mm in figures 9 and 10 respectively. Compared with figure 9(*a*), figure 9(*b*) shows that the downstream evolution of the high-shear layer caused by the roughness alone is completely modified by the mesh

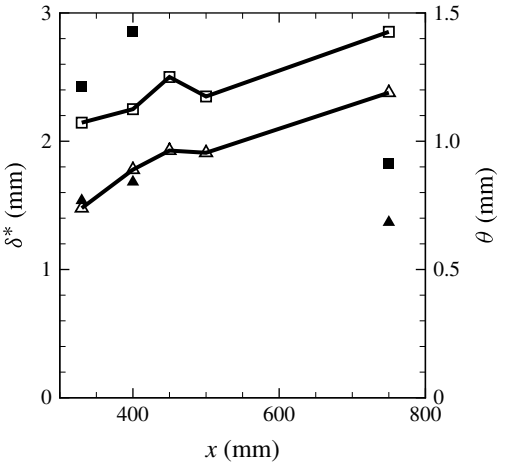

FIGURE 8. Effect of a mesh on the boundary layer integral length scales. For R: □, δ^*; △, θ. For R & LM02mm: ■, δ^*; ▲, θ. The mesh is at $x_m = 450$ mm.

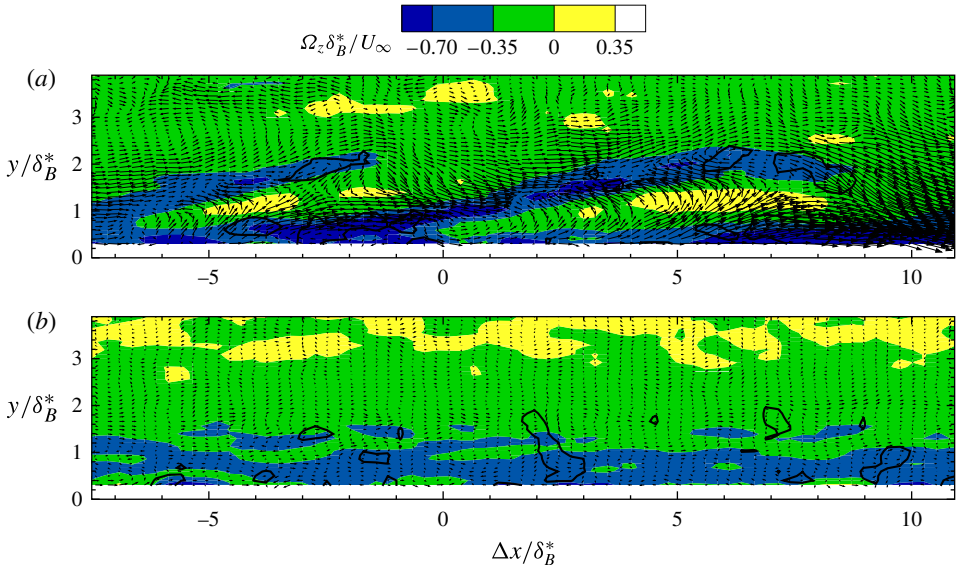

FIGURE 9. (Colour online) Instantaneous spanwise vorticity contours in the wall-normal plane at $x = 750$ mm illustrating the effect of a mesh on roughness-induced transitional flow; the arrows are fluctuating velocity vectors of u and v: (*a*) R; (*b*) R & LM02mm. The line contours represent the normalized swirl strength ($\lambda\delta^*/U_{fs}$); contour level: (*a*) −0.15 and (*b*) −0.1. The wall-normal plane is at $\Delta z/\delta_B^* \approx 0.58$. Note that the inclined high-shear layers caused by roughness in (*a*) are absent due to the mesh in (*b*).

(at $x_m = 450$ mm and $y_m = 2$ mm). The colour contours in figure 9(*b*) are based on δ_B^* and U_∞ (= 5.3 m s^{-1}) values used in the roughness-alone case, for a meaningful comparison. The line contours show the normalized swirl strength, $\lambda\delta^*/U_{fs}$. It can be seen that strong vortices (shown by line contours), which are associated with lifted-up shear layers, are either destroyed or their strength is reduced by the mesh.

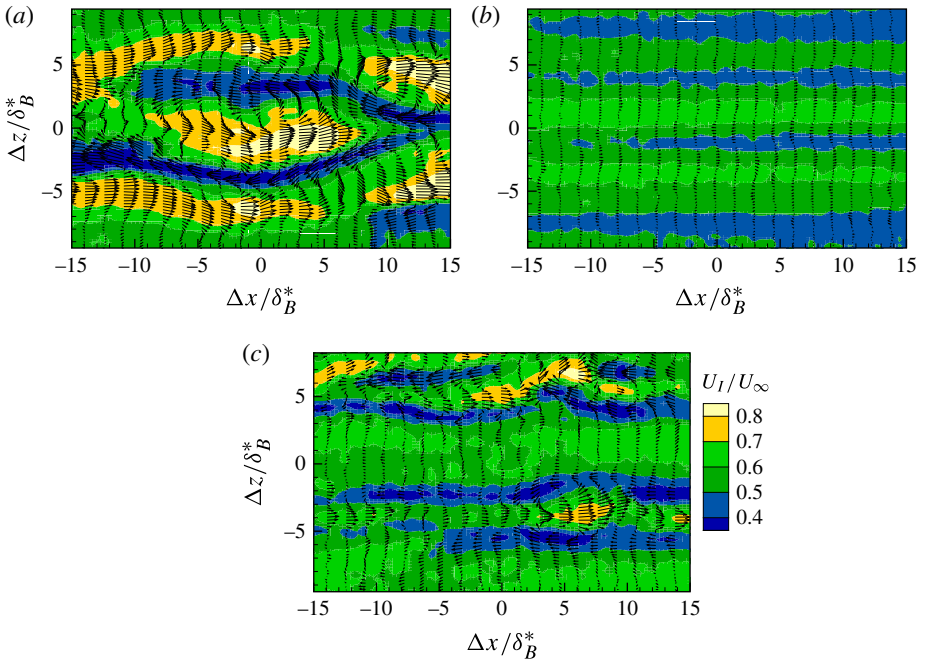

FIGURE 10. (Colour online) Instantaneous streamwise velocity contours in the spanwise plane at $x = 750$ mm illustrating the effect of a mesh on roughness-induced transitional flow: (*a*) R; (b) R & LM02mm; (*c*) R & SM02mm. The arrows are fluctuating velocity vectors of u and w. The spanwise plane is at $y/\delta_B^* \approx 1.84$.

Similarly, the formation of orderly and less intense low- and high-speed streaks due to the mesh can be seen on comparing figure 10(*b*) with figure 10(*a*); we note that the contours in these figures are also based on the U_∞ ($= 5.3$ m s^{-1}) value of the roughness-alone case. Comparing the streak spacing at $x = 750$ mm in figure 10(*b*) with that at $x = 500$ mm (figure 5*b*), it is seen to increase downstream, along with increased streak width. The R_{uu} correlation (not shown here) also revealed the same. The strong disturbances at $\Delta z/\delta_B^* \approx \pm 5$ in figure 10(*c*) are due to the finite mesh width, as mentioned earlier. Therefore, the mesh seems to break up the unsteady activities in the outer high-shear layer region and modify the spanwise structure as well. Interestingly, the lifted-up high-shear layer with negative u fluctuations in figures 3(*a*) and 9(*a*) and the streak breakdown via the varicose instability in figures 3(*b*) and 5(*a*) are similar to those in bypass transition induced by a high level of FST (e.g. Mandal *et al.* 2010; Hack & Zaki 2014). While the mesh at $y_m = 2$ mm modifies many transitional events in the spanwise plane, the shape of the large-scale streamwise structure in the wall-normal plane seems to be more or less preserved, as also discussed in § 3.2 below. This is shown in figure 11 in terms of the contours of R_{uu} at $x = 750$ mm.

3.2. *Effect of a mesh on FST-induced transition*

As mentioned earlier, a grid was used (see figure 1*b*) to create a transitional flow by FST. The measured mean flow characteristics are shown in figure 12; here, δ^* and $u_{rms,max}$ are the local displacement thickness and maximum value of u_{rms}

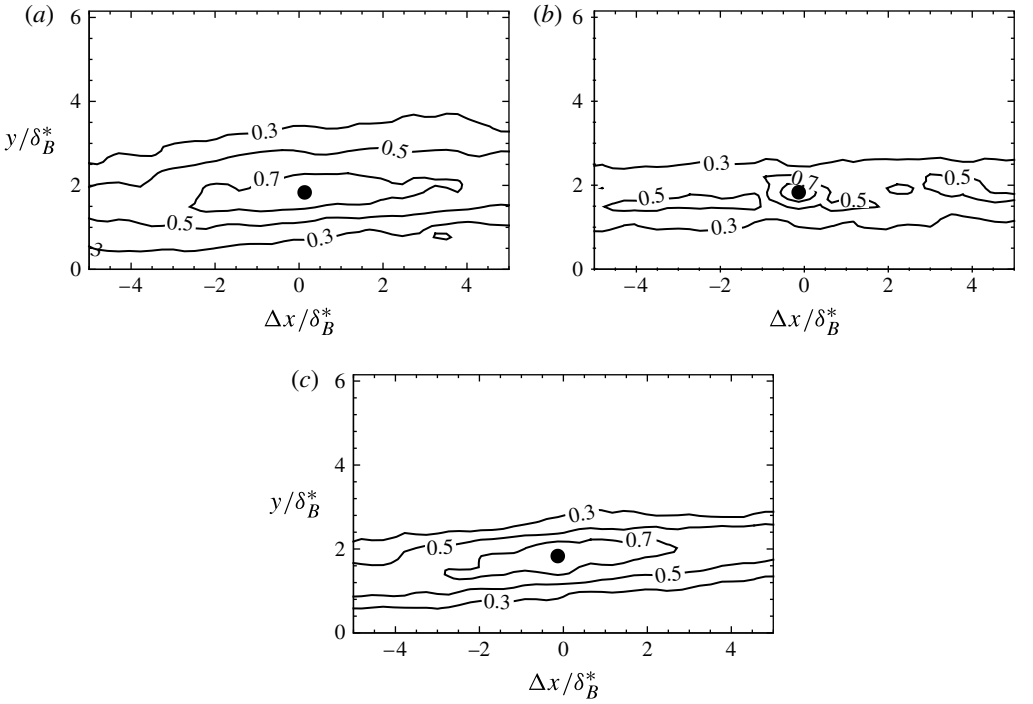

FIGURE 11. Contours of R_{uu} showing the effect of a mesh on roughness-induced transition at $x = 750$ mm and $\Delta z/\delta_B^* \approx 0.58$: (*a*) R; (*b*) R & LM02mm; (*c*) R & SM02mm. The black dot indicates the reference location.

respectively. As in Matsubara & Alfredsson (2001), the boundary layer velocity profiles (figure 12*a*) become fuller in the inner half and show deficit in the outer half of the boundary layer with increasing downstream distance (indicated by an upward/downward arrow). Figure 12(*b*), for pre-transitional flow, shows that the variation of $u_{rms}/u_{rms,max}$ compares well with the non-modal growth of Luchini (2000). The streamwise variations of $u_{rms,max}$ and its wall-normal location in figure 12(*c*) show that $u_{rms,max}$ in pre-transitional flow occurs at approximately $y/\delta^* = 1.3$, and it moves towards the wall with increasing downstream distance (e.g. Westin *et al.* 1994; Matsubara & Alfredsson 2001). The maximum value of u_{rms} at the transition onset ($x = 300$ mm, $\gamma \approx 1.3\,\%$ at $y/\delta^* \approx 1.1$) is approximately $0.12U_\infty$, but its wall-normal location is slightly lower than $y/\delta^* = 1.3$–1.4 reported by others (e.g. Matsubara & Alfredsson 2001; Hernon *et al.* 2007); here, γ is the flow intermittency.

In terms of the probability density function (p.d.f.) of the normalized instantaneous velocity fluctuations, Imayama, Alfredsson & Lingwood (2012) have reported the change in flow structure during transition on a rotating disk. Nolan (2009) and Patten, Griffin & Young (2013) also suggest that such p.d.f. plots provide a good representation of the magnitude of fluctuations at different wall-normal locations in an FST-induced transitional flow. Here, we follow Imayama *et al.* (2012). After normalizing the p.d.f. amplitude at each wall-normal location by its maximum value, such plots for streamwise instantaneous velocity fluctuations at different streamwise locations are shown in figure 13(*a–f*); here, δ is the local boundary layer thickness. Only u fluctuations are considered, as $u \gg v$ in FST-induced transition (e.g. Jacobs &

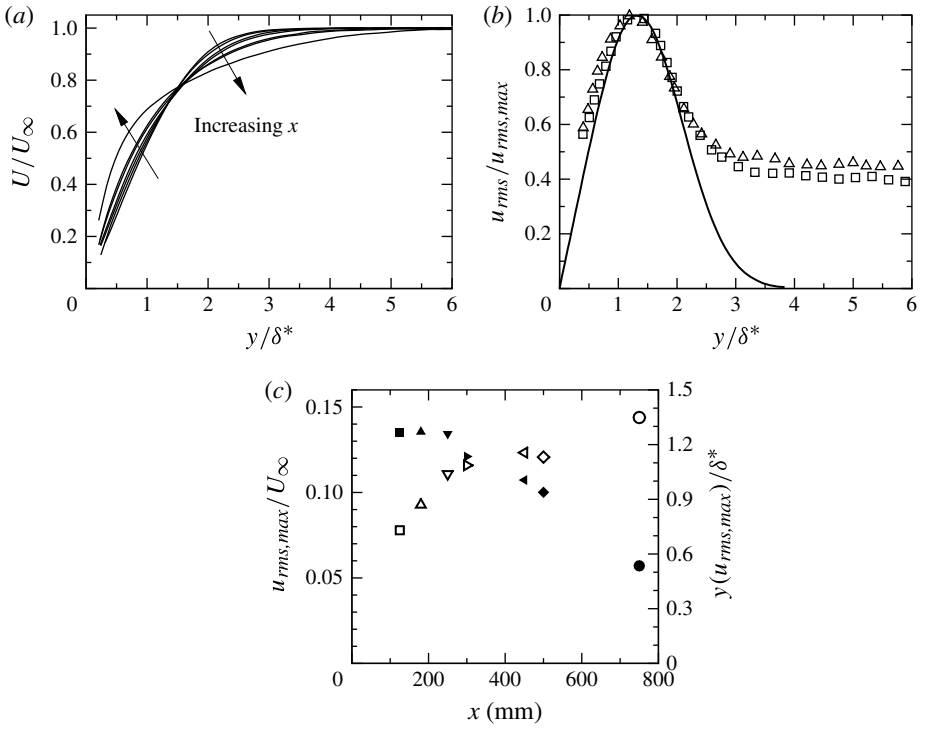

FIGURE 12. Mean flow characteristics in an FST-induced transitional boundary layer. (*a*) Mean velocity profiles; the arrows indicate the downstream change in profile shape. (*b*) Comparison of pre-transitional u_{rms} profiles with Luchini (2000). (*c*) Streamwise variations of $u_{rms,max}$ (empty symbols) and its wall-normal location (filled symbols). Symbols: □, $x = 125$ mm; △, $x = 180$ mm; ▽, $x = 250$ mm; ▷, $x = 300$ mm; ◁, $x = 450$ mm; ◇, $x = 500$ mm; ○, $x = 750$ mm.

Durbin 2001; Mandal *et al.* 2010). The asymmetry in the p.d.f. distributions inside the boundary layer can be attributed to the presence of negative u fluctuations in the inclined shear layer away from the wall and positive u fluctuations in the shear layer close to the wall (e.g. Jacobs & Durbin 2001; Mandal *et al.* 2010; Nolan & Zaki 2013). Downstream, the p.d.f. seems to be more skewed to the left near the boundary layer edge. This might be due to the lifting up of low-speed streaks to the boundary layer edge. The p.d.f. is symmetric in the free stream as the flow is isotropic there. The peak negative velocity fluctuation is higher than the peak positive fluctuation; the increase in their magnitudes and the movement of the peak positive fluctuation towards the wall on approaching the transition onset are in agreement with Hernon *et al.* (2007). The movement of the peak negative fluctuation towards the boundary layer edge is not so clear. At $x = 250$ mm, i.e. near the transition onset, the locations of the peak negative and positive fluctuations at $y/\delta \approx 0.5$ and 0.2 respectively in figure 13(*c*) are also close to those reported by Hernon *et al.* (2007). On approaching the transition onset, two peaks in the p.d.f. plots appear near the location of $u_{rms,max}$. This might be due to the secondary instability of streaks. Imayama *et al.* (2012) have also reported double peaks in p.d.f. plots at the wall-normal location of maximum disturbance in transitional flow on a rotating disk. By conditional sampling of positive and negative u fluctuations (e.g. Kähler 2004), the distributions of $u_{rms,p}$ (for positive

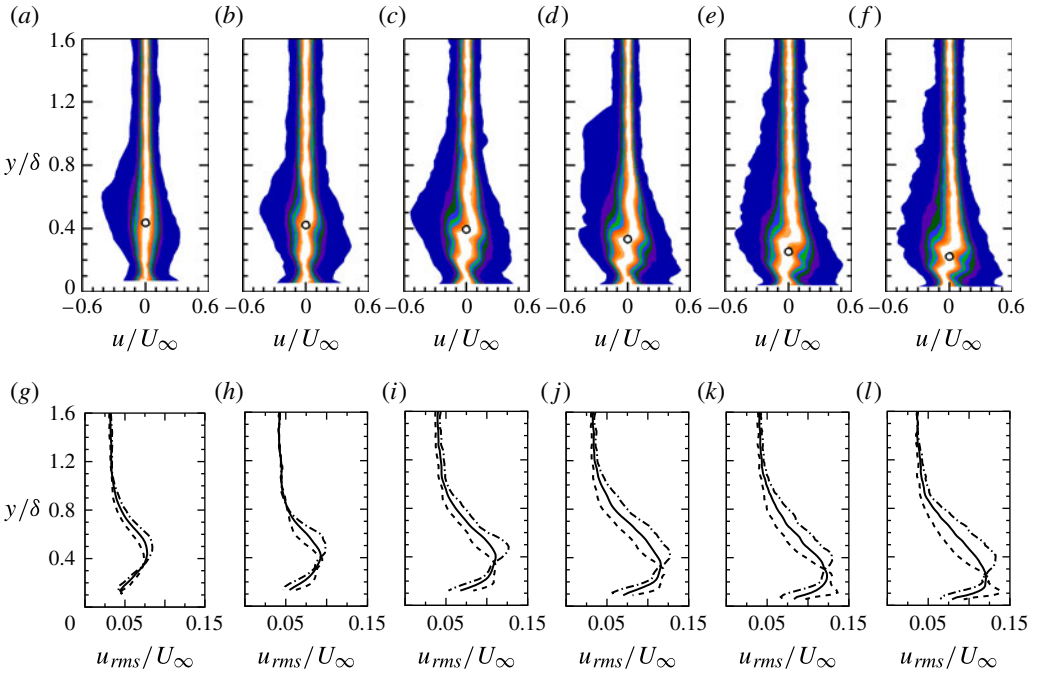

FIGURE 13. (Colour online) Probability density functions of the instantaneous streamwise velocity fluctuation (*a–f*) and corresponding distributions of the root-mean-square values across the boundary layer (*g–l*) at different streamwise locations in FST-induced transitional flow: (*a,g*) $x = 125$ mm; (*b,h*) $x = 180$ mm; (*c,i*) $x = 250$ mm; (*d,j*) $x = 300$ mm; (*e,k*) $x = 450$ mm; (*f,l*) $x = 500$ mm. The empty circle denotes the $u_{rms,max}$ location. Lines: ——, u_{rms}; - - - -, $u_{rms,p}$; — · —, $u_{rms,n}$. Contours levels in (*a–f*): 10 %–90 % of the local p.d.f. value with increment of 10 %.

fluctuation) and $u_{rms,n}$ (for negative fluctuation) are shown in figure 13(*g–l*), along with u_{rms}. It can be seen that the peak values of $u_{rms,p}$ and $u_{rms,n}$ are higher than u_{rms}. Interestingly, the wall-normal locations of peak $u_{rms,p}$ and $u_{rms,n}$ nearly correspond to the peaks of the instantaneous velocity fluctuations in the p.d.f. plots (figure 13*a–f*).

An inclined high-shear layer is always present in FST-induced transition, irrespective of whether a turbulent spot appears at the boundary layer edge (e.g. Jacobs & Durbin 2001; Zaki & Durbin 2005) or at the interface of low- and high-speed streaks (e.g. Nolan & Walsh 2012). A similar inclined high-shear layer was also seen in the instantaneous PIV measurements at $x = 450$ mm (not shown here). Here, again, the mesh was introduced at $x_m = 450$ mm and at different wall-normal locations to study its effect on FST-induced transitional flow, including possible transition delay, as in § 3.1.

The effect of a mesh on the boundary layer flow characteristics at $x = 500$ mm is shown in figure 14; dimensional quantities are shown for clarity. Here (and hereafter), the FST-alone case is denoted by G, and G & LM02mm, G & LM04mm, etc. indicate that LM was placed at $y_m = 2$ mm, 4 mm, etc., in this transitional flow. The mean velocity in figure 14(*a*) shows a mild acceleration near the wall and an overshoot in the outer region, followed by a reduced free-stream velocity. Bi *et al.* (2014) have also reported similar variation of the boundary layer velocity downstream of a flexible net of finite size. Moreover, the velocity overshoot seems to be similar to that

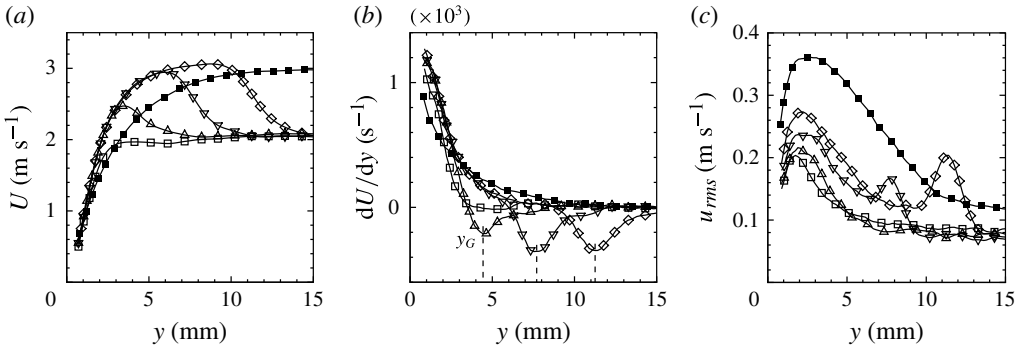

FIGURE 14. Effect of a mesh on the boundary layer flow characteristics at $x = 500$ mm. (*a*) Mean velocity, (*b*) velocity gradient and (*c*) intensity of fluctuation. Symbols: ■, G; □, G & LM02mm; △, G & LM04mm; ▽, G & LM08mm; ◇, G & LM12mm. Here, y_G denotes the location of maximum negative $\mathrm{d}U/\mathrm{d}y$.

observed by He, Pan & Wang (2013) in flow over a flat plate with a cylinder placed above it; the overshoot is much smaller in their case. The large velocity gradients ($\mathrm{d}U/\mathrm{d}y$) near the wall and in the outer region, compared with the FST-alone case, are better seen in figure 14(*b*). The wall-normal location corresponding to the peak of negative $\mathrm{d}U/\mathrm{d}y$ is denoted by y_G. The pressure drop caused by the mesh reduces the free-stream velocity by almost 30 % from $U_\infty = 3$ to 2.1 m s^{-1}, irrespective of its location. This reduction is similar to that in the roughness-induced transition discussed in § 3.1. The velocity overshoot increases rapidly as the mesh is moved from $y_m = 2$ to 8 mm and then slowly for higher mesh location. The variation of u_{rms} in figure 14(*c*) shows a large reduction of it by the mesh, compared with the FST-alone case, and the greatest reduction occurs when the mesh is close to the wall. For the mesh at $y_m > 4$ mm, the large value of u_{rms} in the outer region is due to the large velocity gradient there. Moreover, for the mesh at $y_m \geqslant 4$ mm, the peak u_{rms} near the wall occurs at about the same wall-normal location. Therefore, on introduction of the mesh at $x_m = 450$ mm downstream of the leading edge, the location of peak u_{rms} near the wall is not significantly altered when compared with the FST-alone case.

Typical instantaneous PIV measurements depicting the effect of a mesh near the wall on FST-induced transitional flow at $x = 500$ mm are shown in figure 15. For the FST-alone case, figure 15(*a*) represents a typical breakdown scenario, similar to that reported by Mandal *et al.* (2010). The clockwise vortex (white line) slightly above and to the right of an anticlockwise vortex (black line), and strong negative velocity fluctuations over the positive vorticity region in this figure are similar to those reported by Hladík, Jonáš & Uruba (2011) for a turbulent spot in a non-bypass (natural) type transitional flow. This is possibly expected as the breakdown via turbulent spots may be common in bypass, natural or controlled (by a vibrating ribbon, for example) transition. A similar relative arrangement of clockwise and anticlockwise vortices also prevails in turbulent flows (e.g. Wu & Christensen 2006; Natrajan, Wu & Christensen 2007). Compared with the FST-induced transition case in figure 15(*a*), the mesh at $y_m = 2$ and 4 mm causes the negative spanwise vorticity and clockwise vortices to be confined very close to the wall, as shown in figures 15(*b*) and 15(*c*) respectively; the non-dimensional contours in these figures are based on the δ^* (= 2.86 mm) and U_∞ (= 3 m s^{-1}) values of the FST-alone case. Importantly, the inclined shear layers in figure 15(*a*) are now absent in the presence of a mesh, as was also seen earlier in

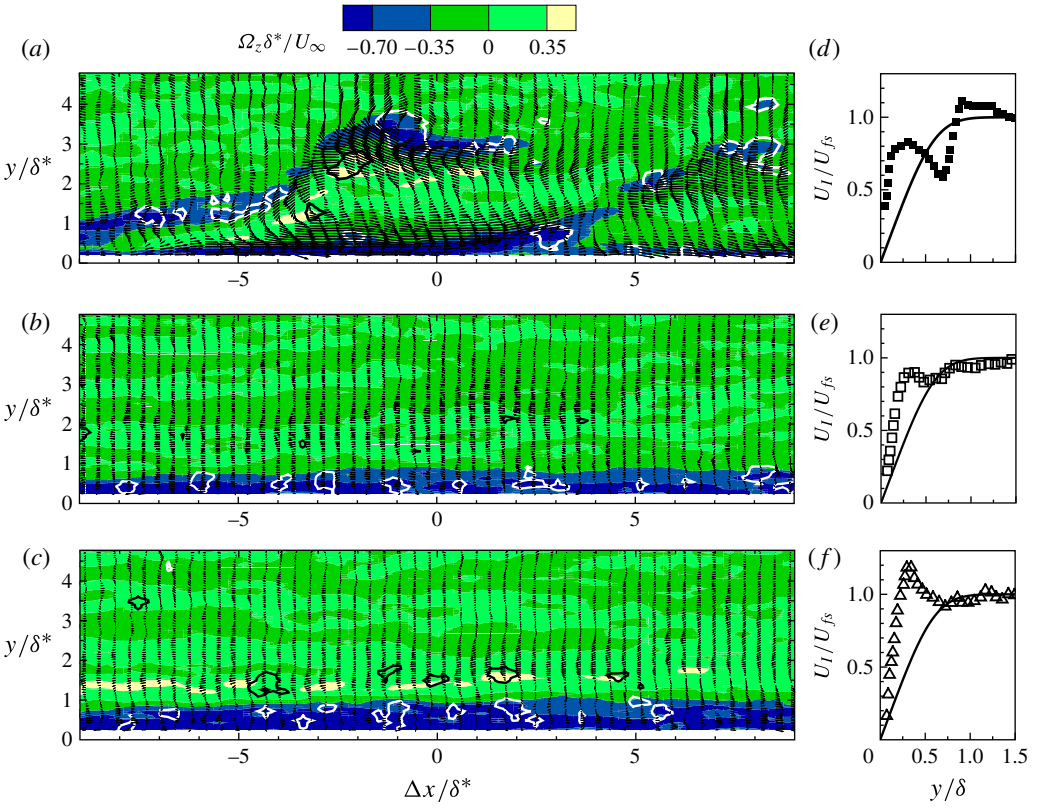

FIGURE 15. (Colour online) Instantaneous spanwise vorticity contours in the wall-normal plane at $x = 500$ mm illustrating the effect of a mesh placed near the wall (*b*,*c*) on FST-induced transitional flow (*a*): (G (*a*); G & LM02mm ($y_m/\delta^* = 0.7$) (*b*); G & LM04mm ($y_m/\delta^* = 1.4$) (*c*)). The arrows are fluctuating velocity vectors of u and v, and the line contours represent the swirl strength (white line, clockwise vortex; black line, anticlockwise vortex). (*d–f*) Comparison of instantaneous velocity profiles at $\Delta x/\delta^* = -1.3$ (in *a–c*) with the Blasius profile (——). Note that the inclined high-shear layers caused by FST alone (*a*) are absent due to LM in (*b*,*c*).

figure 9(*b*), and the velocity fluctuation is also less. Almost 98 % of the instantaneous PIV measurements (in the case of a mesh at $y_m = 2$ mm) were found to be identical to figure 15(*b*); however, being instantaneous, the fluctuating velocity vectors were not of the same sign. The anticlockwise vortices at $y/\delta^* \approx 1.4$ in figure 15(*c*) are those generated by the bottom edge of the mesh at $y_m = 4$ mm. The instantaneous velocity (U_I/U_{fs}) profiles at $\Delta x/\delta^* = -1.3$ in figure 15(*a–c*) are compared with the Blasius profile in figure 15(*d–f*); note that δ and U_{fs} are the local values. These clearly show acceleration near the wall. Noting the absence of inclined high-shear layers in figure 15(*b*,*c*), the large reduction of u_{rms} by the mesh at $y_m = 2$ and 4 mm (figure 14*c*) is due to the suppression of such shear layers and the associated transitional structure.

Figure 16 shows some typical instantaneous PIV measurements in flows with the mesh away from the wall at $y_m = 8$ and 12 mm; the non-dimensional contours in these figures are also based on the δ^* (= 2.86 mm) and U_∞ (= 3 m s^{-1}) values of the FST-alone case. We note that figures 16(*b*) and 16(*c*) are representative of two

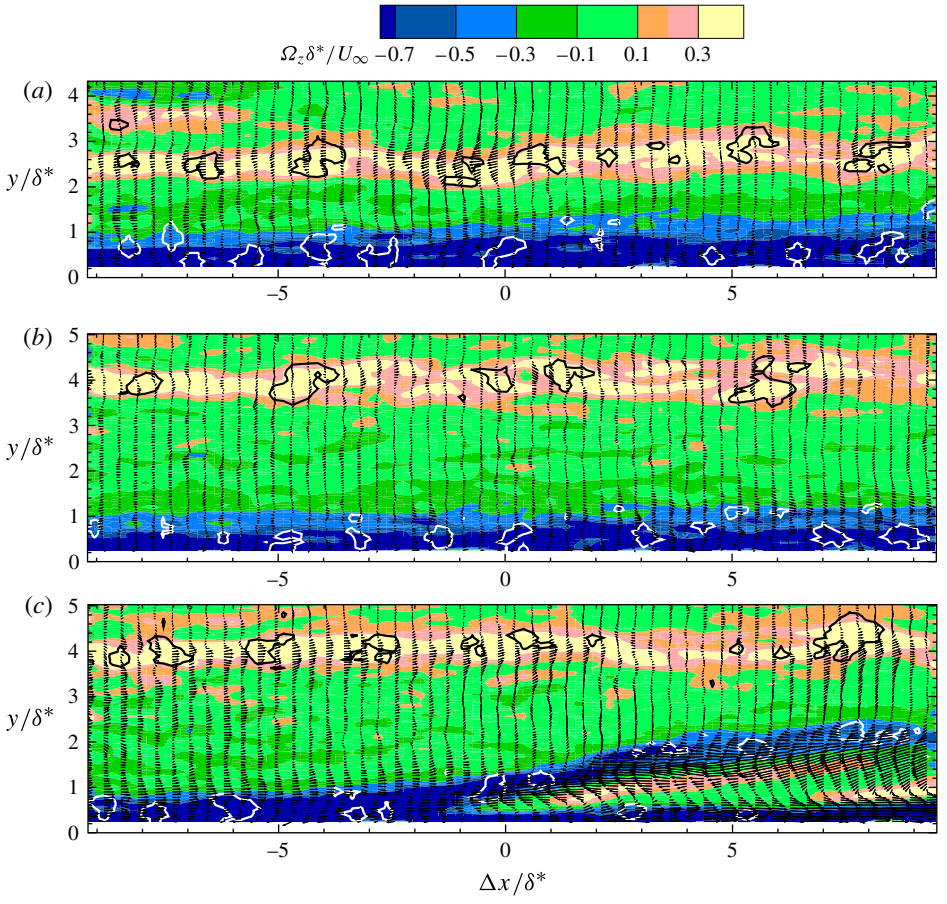

FIGURE 16. (Colour online) Instantaneous spanwise vorticity contours in the wall-normal plane at $x = 500$ mm illustrating the effect of a mesh located away from the wall on FST-induced transitional flow: (*a*) G & LM08mm ($y_m/\delta^* = 2.8$); (*b*,*c*) G & LM12mm ($y_m/\delta^* = 4.2$). The arrows are the fluctuating velocity vectors of u and v. The line contours represent the swirl strength (white line, clockwise vortex; black line, anticlockwise vortex). Note that shear layer is near the wall in (*a*,*b*) while it is inclined in (*c*).

different events – a large shear near the wall and a lifted-up shear layer. Figure 16(*a*) shows that strong negative spanwise vorticity and clockwise vortices are confined close to the wall, similar to those in figures 15(*b*) (for $y_m = 2$ mm) and 15(*c*) (for $y_m = 4$ mm). The number of such PIV frames was found to decrease with increasing y_m. For example, although similar instantaneous PIV measurements were found for the mesh at $y_m = 12$ mm (figure 16*b*), the lifted-up shear layer (figure 16*c*) and breakdown, similar to those for FST-induced transition (figure 15*a*), were found to be greater; the only difference was the presence of anticlockwise vortices in the free stream. Figure 16(*c*) then suggests that the lift-up of the high-shear layer in FST-induced transition is not entirely suppressed by a mesh placed away from the wall even though it reduces the free-stream velocity by 30 % and accelerates the flow (figure 14*a*). Consequently, the higher u_{rms} inside the boundary layer in flow with the mesh at $y_m = 12$ mm (figure 14*c*) is due to transitional flow that prevails there. Therefore, unless the lift-up is disturbed, as in the case of the mesh at $y_m = 2$ and

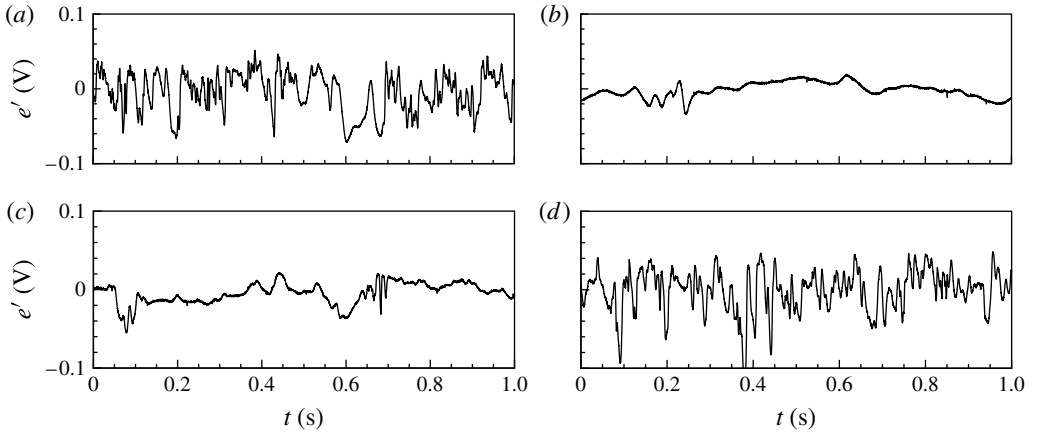

FIGURE 17. Hot-wire signals at $x = 750$ mm showing the effect of a mesh at different wall-normal locations on FST-induced transition: (*a*) G; (*b*) G & LM02mm; (*c*) G & LM04mm; (*d*) G & LM12mm.

4 mm, by manipulating the outer region, transition delay over a large downstream distance may not be possible, even with a reduced free-stream velocity and flow acceleration.

The hot-wire signals at $x = 750$ mm in figure 17 show the effect of the mesh at different y_m locations; here, e' is the voltage fluctuation and t is the time in seconds. These signals were taken at the wall-normal location corresponding to $u_{rms,max}$. Figure 17(*b*) shows that the mesh at ($x_m = 450$ mm and) $y_m = 2$ mm inhibits the high-frequency fluctuations seen in figure 17(*a*). In fact, figure 17(*b*) is a typical low-intermittency signal (between 0.15 to 0.25 s) associated with the passage of incipient turbulent spots. Thus, compared with the FST-alone case in figure 17(*a*), one finds that transition delay has been caused by the mesh at $y_m = 2$ mm. However, this does not occur for the mesh at $y_m > 8$ mm, and high-frequency fluctuations still persist (figure 17*d*). The flow intermittency increases with increasing y_m.

The mean flow characteristics in the boundary layer at $x = 750$ mm are shown in figure 18. Corresponding to the hot-wire signal in figure 17(*a*), the boundary layer velocity profile is compared with the (1/7)th power law for turbulent flows in figure 18(*a*); $H\,(= \delta^*/\theta)$ denotes the shape factor. It can be seen that the flow due to FST is not fully turbulent yet. Figure 18(*b*) shows that, although the near-wall acceleration is reduced, the velocity overshoot persists even at $x = 750$ mm. Interestingly, the velocity profile corresponding to the hot-wire signal in figure 17(*b*) is a near-Blasius one, as shown in figure 18(*c*). That is, the mesh at $y_m = 2$ mm has caused a near relaminarization of the FST-induced transitional flow; this also reflects in lower fluctuation intensities in flows with the mesh at $y_m = 2$ and 4 mm than the FST-alone case (figure 18*d*), even 300 mm downstream of the mesh. This may be due to the fact that as the upper part of the transitional boundary layer is affected by the mesh, a rapid recovery of streamwise streaks is prevented, unlike in the control of streaks near the wall (e.g. Lundell 2007; Monokrousos *et al.* 2008). For the mesh at $y_m = 12$ mm, the peak u_{rms} value is slightly greater than in the FST-alone case, possibly indicating a faster transition due to the increased disturbances in the outer region by the mesh.

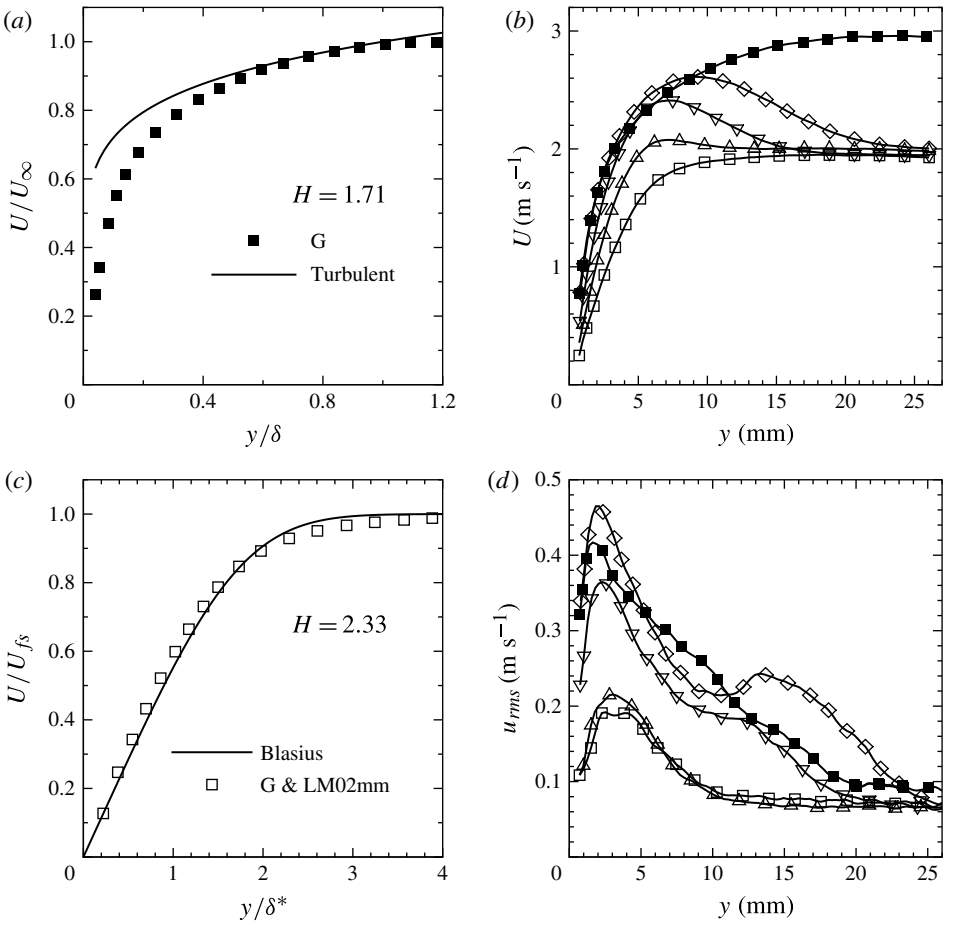

FIGURE 18. Mean flow characteristics at $x = 750$ mm. (*a*) Comparison of the boundary layer velocity profile with the (1/7)th profile for turbulent flows. The measured profile corresponds to the hot-wire signal in figure 17(*a*). (*b*) Effect of a mesh on boundary layer velocity profiles. (*c*) Comparison of the measured boundary layer velocity profile corresponding to the hot-wire signal in figure 17(*b*) with the Blasius profile. (*d*) Effect of a mesh on the intensity of fluctuations. The symbols are as in figure 14.

Along with a reduction of the free-stream velocity (figures 14*a* and 18*b*), transition delay caused by the mesh also reduces the integral length scales like θ and δ^*; therefore, there is a reduction in the flow Reynolds number. Although we have not measured the skin friction, we consider the low-intermittency flow in figure 17(*b*), for the mesh at $y_m = 2$ mm, to infer the skin-friction coefficient, C_f, using the transition zone model of Dhawan & Narasimha (1957). The skin friction in this linear combination model is, $C_f = C_{f,L}(1 - \gamma) + \gamma C_{f,T}$, where the subscripts L and T denote the laminar and turbulent states respectively. For the hot-wire signal in figure 17(*b*), $\gamma \to 0$. Thus, one expects a reduction in C_f during the delay of transition by the mesh at $y_m = 2$ mm.

Figure 19 shows the effect of a mesh on the Reynolds stresses, $\overline{uv}$, $\overline{vv}$, and the turbulence production, $-\overline{uv}\,\mathrm{d}U/\mathrm{d}y$, $-\overline{vv}\,\mathrm{d}U/\mathrm{d}y$, at $x = 500$ mm. It can be seen that, compared with the FST-alone case (filled squares), a mesh reduces these quantities in

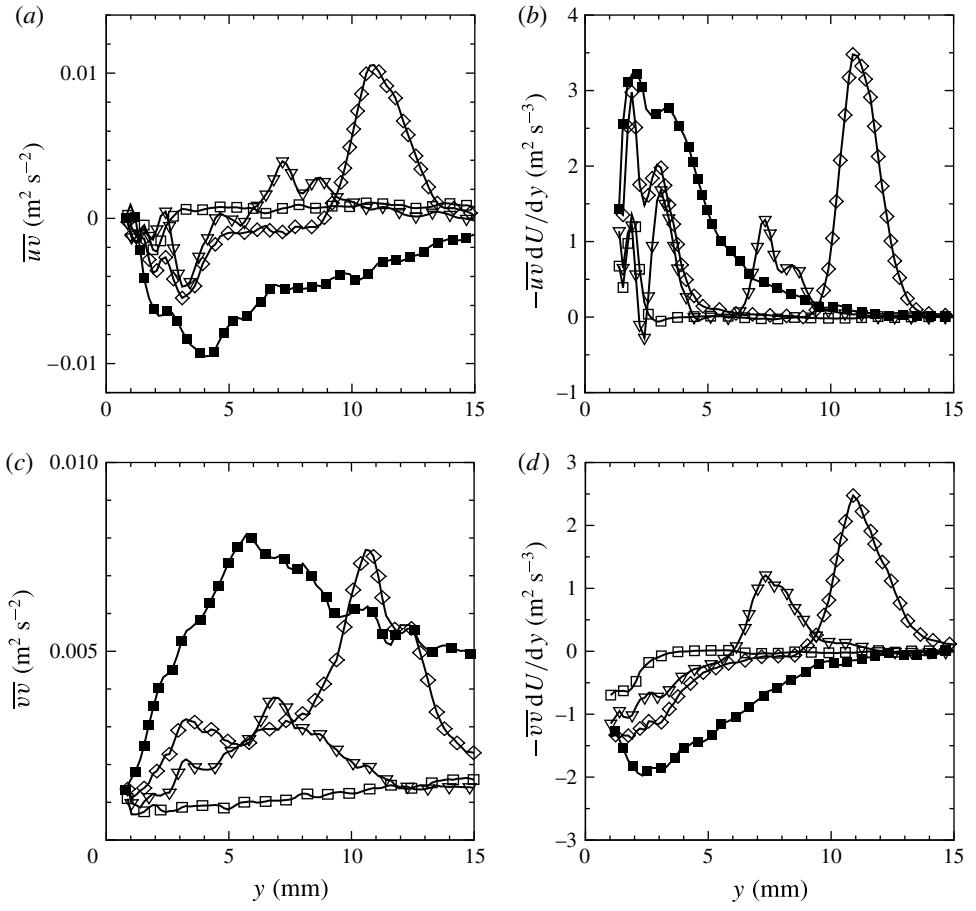

FIGURE 19. Effect of a mesh on the Reynolds stresses and turbulence production at $x = 500$ mm: (*a*) $\overline{uv}$, (*b*) $-\overline{uv}\,\mathrm{d}U/\mathrm{d}y$, (*c*) $\overline{vv}$ and (*d*) $-\overline{vv}\,\mathrm{d}U/\mathrm{d}y$. The symbols are as in figure 14.

the boundary layer, and the greatest reduction occurs with the mesh at $y_m = 2$ mm. As the mesh is moved away from the wall, Reynolds stresses and turbulence production increase considerably in the outer region due to the large velocity gradient there (see figure 14*b*). The variations of these quantities in the wall and outer regions with increasing y_m are similar to those for u_{rms}, described above. Moreover, quadrant decomposition of the Reynolds shear stress (Wallace, Eckelmann & Brodkey 1972) shows a reduction of this during Q_2 (ejection: $-u$, v) and Q_4 (sweep: u, $-v$) events, as shown in figures 20(*b*) and 20(*d*) respectively. For the FST-alone case, the peak value of $\overline{uv}$ in Q_2 is in the middle of the boundary layer, and it is close to the wall in Q_4, as in Nolan, Walsh & McEligot (2010); however, near the wall, $\overline{uv}$ in Q_3 is different from these authors. While the mesh at all y_m locations reduces these events, the maximum reduction is again for the mesh at $y_m = 2$ mm. With increasing y_m, Reynolds stresses in Q_1 (u, v) and Q_3 ($-u$, $-v$) increase rapidly in the outer region in the same way as in figure 19(*a*). The reduction in the turbulence production and Reynolds stresses by the mesh at $y_m = 2$ mm can be attributed to the absence of lifted-up low-speed streaks or interaction between inclined low- and high-speed

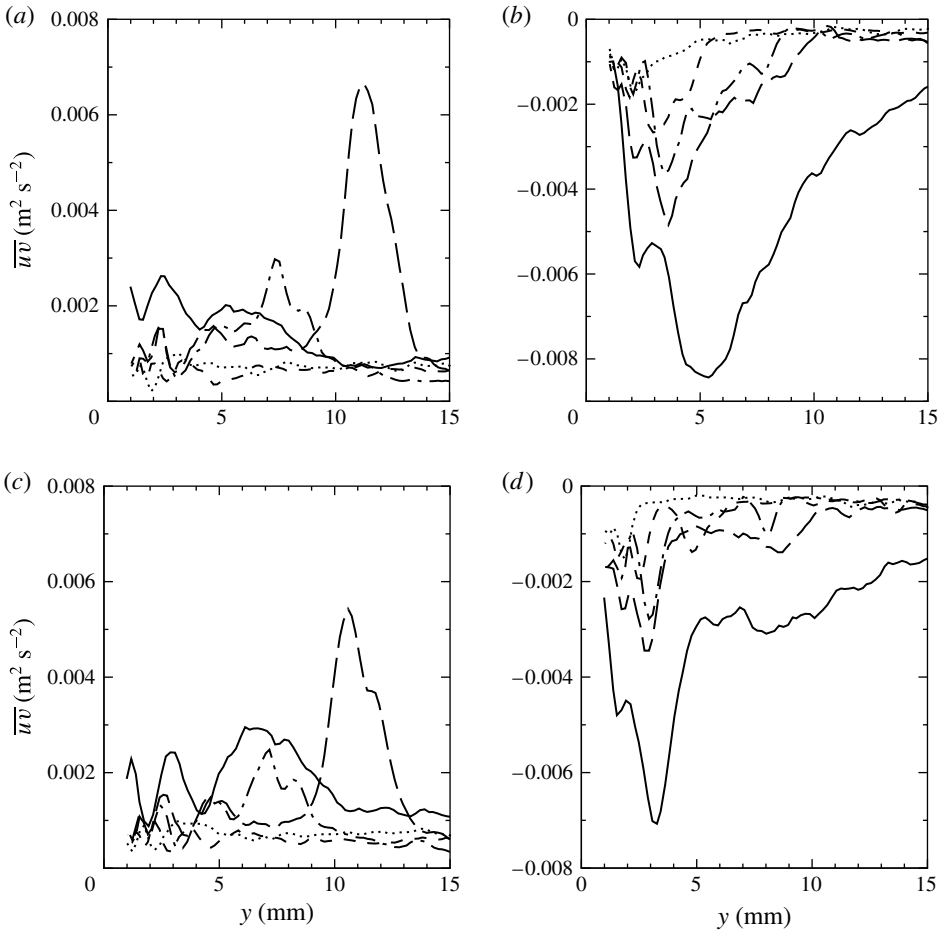

FIGURE 20. Effect of a mesh on the quadrant decomposed Reynolds shear stress at $x =$ 500 mm: (*a*) Q_1 (u, v), (*b*) Q_2 (ejection: $-u,\ \ v$), (*c*) Q_3 $(-u, -v)$ and (*d*) Q_4 (sweep: $u, -v$). Lines: ——, G; · · · · · ·, G & LM02mm; - - - -, G & LM04mm; — · —, G & LM08mm; — — — —, G & LM12mm.

streaks (figure 15*b*) and the associated transitional events. On the other hand, the increased Reynolds shear stress in the boundary layer (during Q_2 and Q_4 events) with increasing y_m is due to the prevailing transitional flows, as discussed earlier (in the context of figure 16).

In a turbulent boundary layer, hairpin vortices contribute to the Reynolds stresses (e.g. Ganapathisubramani, Longmire & Marusic 2003; Tomkins & Adrian 2003; Guala, Hommema & Adrian 2006). Here, a mesh is seen to reduce these stresses in the wall region and increase them in the outer region as it is moved away from the wall, along with a reduction of the free-stream velocity. Thus, it may be worthwhile to find out the effect of a mesh on the population of vortices in the boundary layer. Following Volino, Schultz & Flack (2007), who compare smooth- and rough-wall turbulent boundary layers in terms of the swirl strength, such a quantification is shown in figure 21; for clarity, the two cases of mesh at $y_m = 4$ and 12 mm are shown separately in figure 22. Here, of the total number of PIV frames acquired,

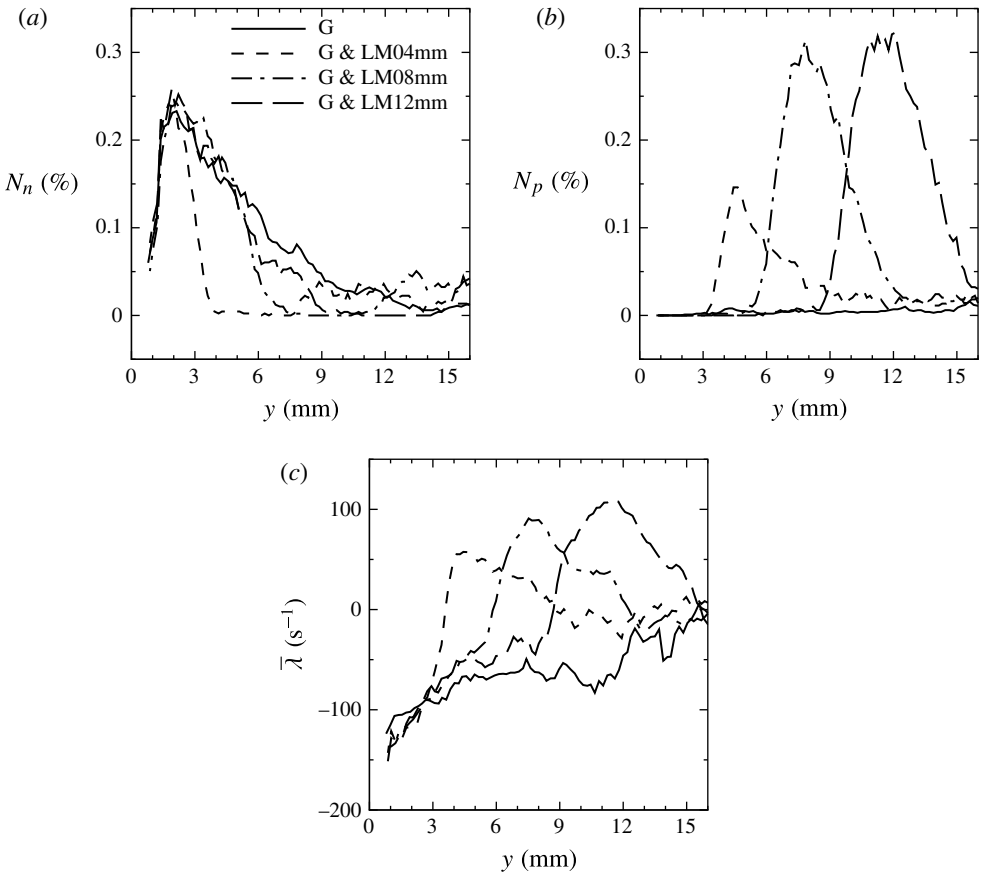

FIGURE 21. Fraction of PIV frames with negative (*a*) and positive (*b*) swirl strength at $x = 500$ mm. (*c*) Mean non-zero swirl strength.

those associated with only negative (N_n) and positive (N_p) swirl strength are counted separately at each wall-normal location at $x = 500$ mm, and are shown as a fraction of the total number of frames; λ_n and λ_p are the corresponding mean swirl strengths, and $\overline{\lambda} = (\lambda_n N_n + \lambda_p N_p)/(N_n + N_p)$. Figure 21(*a*) shows that the mesh at $y_m = 4$ mm reduces the number of PIV frames associated with negative swirl strength (i.e. the population of clockwise vortices) in the outer region and confines them to a very small region close to the wall, compared with the FST-alone case. In other words, clockwise vortices are confined close to the wall by the mesh at $y_m = 4$ mm, as also seen in figure 15(*c*). For $y_m > 4$ mm, although the number of such frames increases with increasing y_m, it is still lower than the FST-alone case. This is due to the prevalence of transitional flows when the mesh is away from the wall. It is also interesting to note that N_n is maximum (i.e. the highest population of clockwise vortices) near the wall at approximately $y = 2$ mm, irrespective of the type of flow; this location nearly corresponds to the maximum of u_{rms} (see figure 14*c*). This might be due to the absence of the leading-edge effect, as the mesh was placed downstream. Moreover, different mean velocity profiles caused by the mesh at $y_m \geqslant 4$ mm do not seem to affect this near-wall result. In other words, the number of vortices with negative swirl strength seems to be almost fixed by the leading-edge effect arising from FST alone.

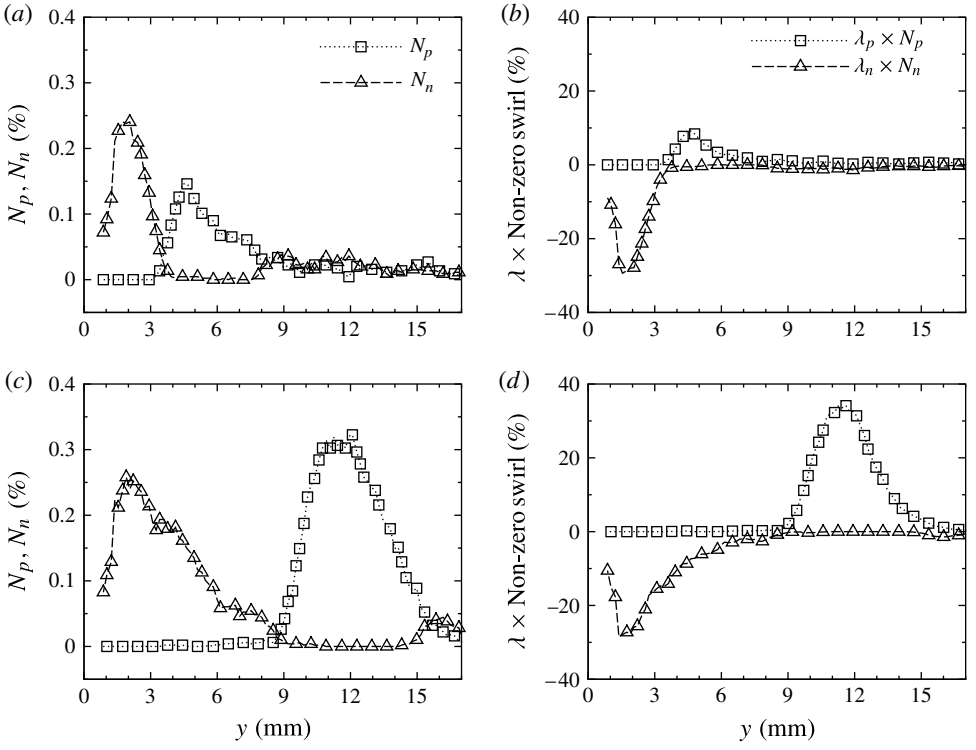

FIGURE 22. Fraction of PIV frames with positive and negative swirl strength at $x =$ 500 mm for a mesh at $y_m = 4$ mm (a) and $y_m = 12$ mm (c). The corresponding products with their mean swirl strengths are shown in (b) and (d) respectively.

Figure 21(b) shows that, while the number of PIV frames with positive swirl strength (i.e. the population of anticlockwise vortices) is negligible across the boundary layer for the FST-alone case, the effect of a mesh on N_p appears only when it is away from the wall, as also observed in instantaneous PIV measurements in figures 15(c) and 16, and the maximum of such vortices occurs at approximately y_G. A mesh in the region $4 \leqslant y_m \leqslant 8$ mm causes an increase in the number of these anticlockwise vortices before attaining an almost constant value. For $y_m \geqslant 8$ mm, the fraction of PIV frames with positive swirl strength is more than those with negative swirl strength. Figure 21(c) shows the variation of the mean non-zero swirl strength ($\overline{\lambda}$) across the boundary layer. Here again, the near-wall feature is the same, irrespective of the mesh location, and its change away from the wall is due to the positive swirl shown in figure 21(b). Thus, suppression of the lift-up of the high-shear layer (and associated transitional events) by the mesh when placed near the wall causes clockwise vortices to be confined to the wall region. Otherwise, apart from a small change in the clockwise vortices, the anticlockwise vortices formed at the bottom edge of the mesh become significant in the outer region.

The p.d.f. plots of the normalized instantaneous u fluctuations in figure 23 show the change in flow structure at $x = 500$ mm by the mesh. The non-dimensional quantities are based on the δ (= 12 mm) and U_∞ (= 3 m s^{-1}) values of the FST-alone case, for a meaningful comparison. The reduced spread of the p.d.f. across the boundary layer in figure 23(b), compared with the FST-alone case in figure 23(a), further confirms

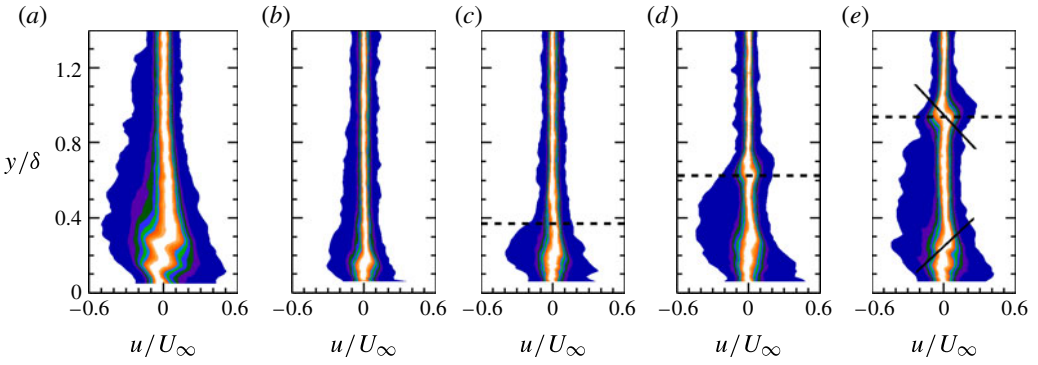

FIGURE 23. (Colour online) Probability density functions of the instantaneous streamwise velocity fluctuations at $x = 500$ mm for various mesh locations. The dashed line indicates the y_G location: (*a*) G; (*b*) G & LM02mm; (*c*) G & LM04mm; (*d*) G & LM08mm; (*e*) G & LM12mm. The contour levels are as in figure 13.

the transition delay caused by the mesh at $y_m = 2$ mm; for the other mesh locations, decreased spread of the p.d.f. near the wall can be seen in figure 23(*c–e*). As y_m increases, the negative p.d.f. region away from the wall also increases. This might be due to the lift-up of the high-shear layer not being entirely suppressed (figure 16). Two clear peaks in the p.d.f. appear near y_G (indicated by a dashed line) for the mesh at $y_m = 8$ and 12 mm; at y_G, the maximum number of anticlockwise vortices (figure 21*b*) and a second peak in u_{rms} (figure 14*c*) appear. As shown in figure 23(*e*), the line connecting two peaks near the wall and a similar line at y_G are almost perpendicular to each other. From the direction of the inclination of these lines, one may infer from a p.d.f. plot itself whether clockwise or anticlockwise vortices are dominant at those locations.

In the relaminarization process of a turbulent boundary layer by a strong streamwise pressure gradient (Blackwelder & Kovasznay 1972) and in near-wall control of FST-induced transition (Lundell 2007), the shape of the spanwise structure is not altered. This may not be so downstream of the mesh, as orderly streaks, similar to those in figure 5(*b*) for the roughness-induced transition, will occur. However, the streamwise structure in the wall-normal plane in FST-induced transition seems to be preserved even in the presence of a mesh, as indicated by the R_{uu} contours at $x = 500$ mm in figure 24; correlation contours at two different reference locations (indicated by black dots) are shown in this figure. Although the mesh seems to distort the streamwise structure slightly when located close to the wall, its overall shape is largely unchanged. The mild increase in size and inclination of the streamwise structure with increasing y_m (figure 24*c–e*) might be due to the reduced effect of acceleration on transitional flow events. From the cross-correlation between 'wall wire' and streamwise velocity fluctuations, Lundell (2007) reports that the size of the structure decreases mainly near the wall in control of an FST-induced transition, but the overall shape seems to remain similar. Elsewhere, Dixit & Ramesh (2010) find that in a turbulent boundary layer subjected to high acceleration, the streamwise structure elongates with decreasing inclination towards the wall. However, the shape seems to be preserved in this case as well. In the case of a mesh at $y_m \geqslant 8$ mm, the weak negative correlation region might be due to the interaction or presence of vortices of opposite sign. On the whole, the shape of the streamwise structure in the wall-normal plane is largely preserved even

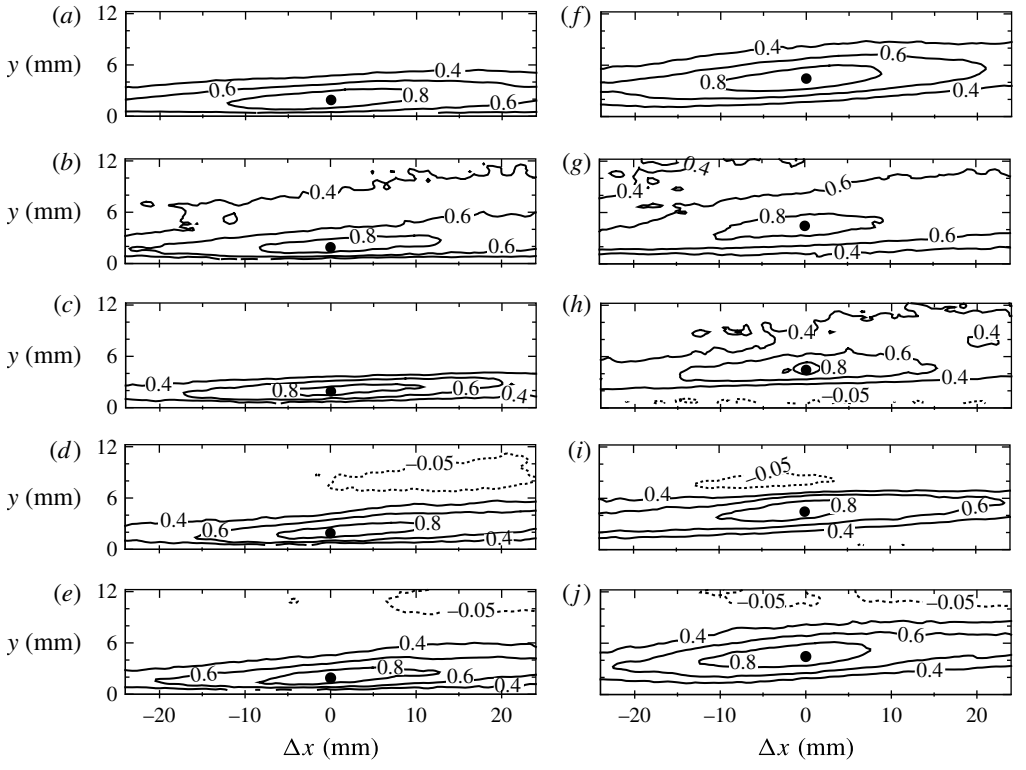

FIGURE 24. Contours of R_{uu} at $x = 500$ mm: (*a,f*) G; (*b,g*) G & LM02mm; (*c,h*) G & LM04mm; (*d,i*) G & LM08mm; (*e,j*) G & LM12mm. The black dot indicates the reference location; note that the reference locations in (*a–e*) and (*f–j*) are different.

in the presence of a mesh, with possibly mild change in size and inclination, as in flows with a mesh in roughness-induced transition (figure 11).

Figure 25 shows the correlation of signed swirl strength with itself, $R_{\lambda\lambda}$, and unsigned swirl strength with the wall-normal velocity fluctuation, $R_{\lambda v}$, at $x = 500$ mm; the reference location ($\Delta x = 0$, $y = y_G$) is indicated by an empty circle. Although such correlations in a turbulent boundary layer correspond to hairpin vortices (e.g. Christensen & Adrian 2001; Volino *et al.* 2007), here they refer to vortices generated by the bottom edge of the mesh (see figures 15*c* and 16). While the correlation contours of $R_{\lambda\lambda}$ compare the size of these vortices and separate the regions of clockwise and anticlockwise vortices in the entire measurement area, the $R_{\lambda v}$ correlation compares the spatial extent and strength of the velocity field associated with them. Figures 25(*a*) and 25(*b*) show $R_{\lambda\lambda}$ contours for the mesh at $y_m = 4$ and 12 mm respectively, whereas figure 25(*c*) shows a comparison of its wall-normal variation at $\Delta x = 0$ for different y_m. As only anticlockwise vortices are present at y_G (figure 21), the regions associated with anticlockwise and clockwise vortices in these contour maps are indicated by positive and negative correlation values respectively. These show that the entire measurement region can be separated into two distinct regions of negative (near the wall) and positive (around y_G) swirl. The strong negative correlation region seen around $y = 2$ mm corresponds to the wall-normal location having the maximum number of vortices with negative swirl strength (figure 21*a*). The larger positive correlation region ($R_{\lambda\lambda} > 0.4$) for $y_m = 12$ mm in figure 25(*b*)

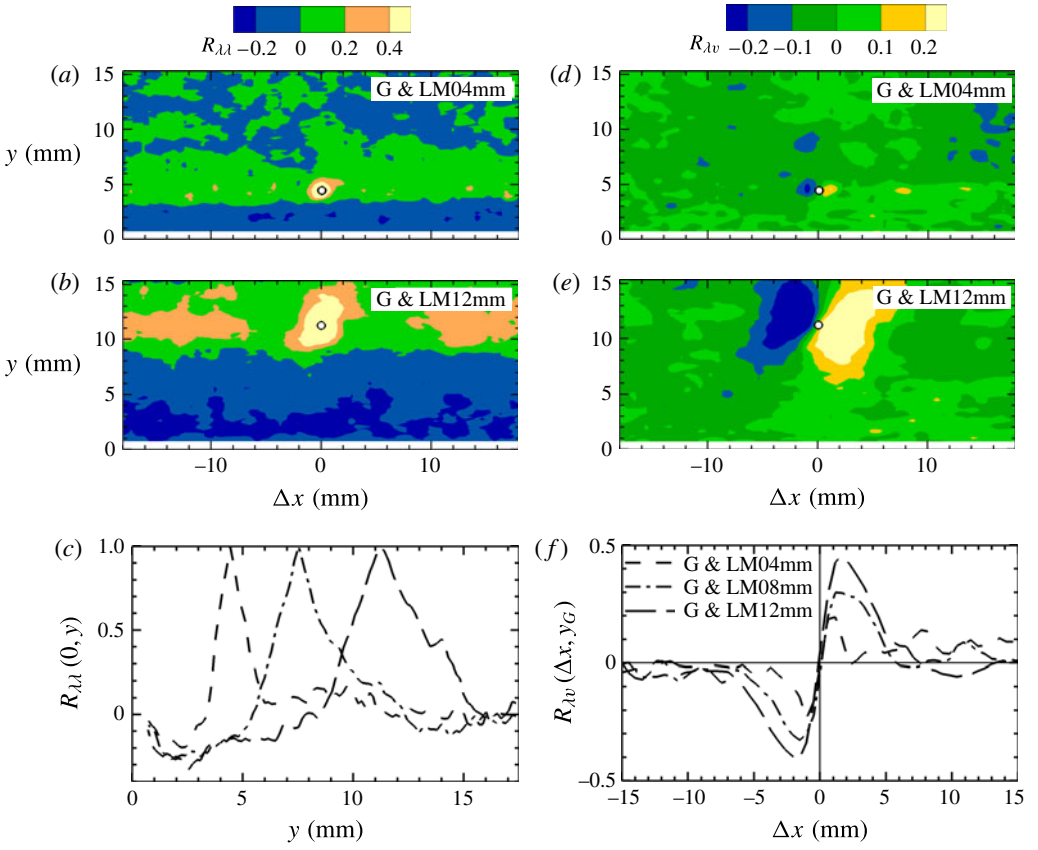

FIGURE 25. (Colour online) Swirl correlations at $x = 500$ mm: (*a*,*b*) $R_{\lambda\lambda}$ contours; (*d*,*e*) $R_{\lambda v}$ contours. Wall-normal variation of $R_{\lambda\lambda}$ at $\Delta x = 0$ (*c*) and streamwise variation of $R_{\lambda v}$ at y_G (*f*) for different y_m. The empty circle denotes the reference location ($\Delta x = 0$, $y = y_G$).

indicates a larger vortex than that for $y_m = 4$ mm (figure 25*a*). Figure 25(*c*) also shows an increase in length of the positive and negative correlation regions with increasing y_m. Figures 25(*d*) and 25(*e*) show $R_{\lambda v}$ contours for the mesh at $y_m = 4$ and 12 mm respectively, while its streamwise variation at y_G for different y_m is shown in figure 25(*f*). The positive and negative correlation regions to the right and left of the reference location in these plots indicate the presence of an anticlockwise vortex. Similar correlation regions below and above the reference location were also seen in $R_{\lambda u}$ plots (not shown here). While the positive and negative correlation regions ($R_{\lambda v} > \pm 0.1$) are small for $y_m = 4$ mm (figure 25*d*), these are significant for $y_m = 12$ mm (figure 25*e*). The weak correlation regions in figure 25(*d*) can be attributed to the fact that the mesh at $y_m = 4$ mm is partly inside the boundary layer and also to the smaller size (figure 25*a*), strength (figure 21*c*) and number (figure 21*b*) of vortices, compared with the mesh at $y_m = 12$ mm. Figure 25(*f*) also shows maximum and minimum values of the correlation and their streamwise spacing increase with increasing y_m. This indicates that the spatial extent and strength of the velocity field associated with the anticlockwise vortex increase as the mesh is moved away from the wall.

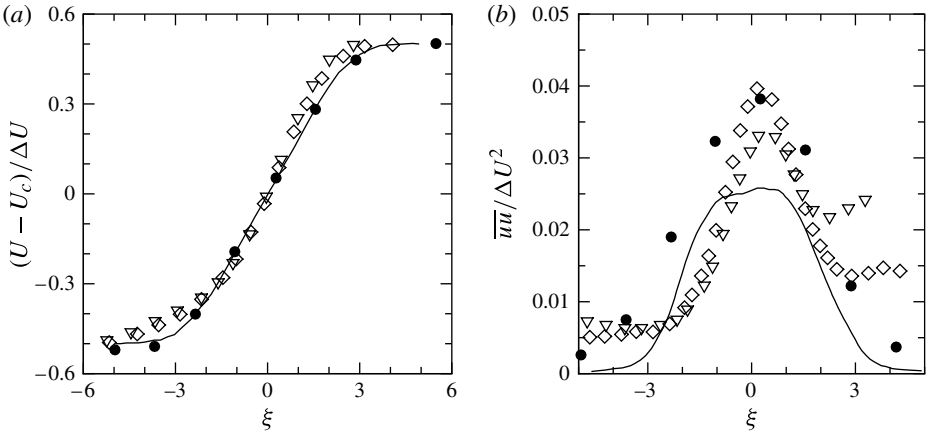

FIGURE 26. The plane mixing layer feature in the outer region of the boundary layer at $x = 500$ mm for the mesh at $y_m = 8$ ($\triangledown$) and 12 ($\diamond$) mm. (*a*) Mean velocity. (*b*) Reynolds stress of the streamwise velocity fluctuations. Mixing layer data: ——, Rogers & Moser (1994); ●, Loucks & Wallace (2012) for $Re_{\theta^*} = 432$.

As noted earlier, the mesh reduces the free-stream velocity and accelerates the boundary layer flow, even causing an overshoot when located away from the wall (figure 14*a*). Now the mesh is expected to cause a mixing layer type discontinuity near its bottom edge, and this effect may continue downstream. It is found that, in flows with the mesh at $y_m = 8$ and 12 mm, the mean velocity profile between the overshoot and free stream at $x = 500$ mm is of the plane mixing layer type reported by Rogers & Moser (1994) and Loucks & Wallace (2012), as shown in figure 26(*a*). Here, following these authors, the similarity variables used are $U_c = (U_p + U_l)/2$ and $\Delta U = U_p - U_l$; U_p is the peak velocity, and $U_l = U_{fs}$; $\theta^* = \int_{-(y_l - y_c)}^{-(y_p - y_c)} [(1/4) - ((U - U_c)/\Delta U)^2]\,\mathrm{d}y$ and $\xi = -(y - y_c)/\theta^*$; $y_c = y(U = U_c)$, $y_p = y(U = U_p)$ and $y_l = y(U = U_l)$; ξ is negative here due to the opposite sense of low- and high-speed fluids from those in Rogers & Moser (1994) and Loucks & Wallace (2012). Similarly, the Reynolds stress, $\overline{uu}/\Delta U^2$, variation in this region also compares well with those reported by these authors (figure 26*b*). This mixing layer feature could be the reason why vortices from the bottom edge of the mesh remain prominent downstream of $x_m = 450$ mm, as shown in figures 15(*c*) and 16. However, it should be noted that there was no wall effect in the studies of Rogers & Moser (1994) and Loucks & Wallace (2012); in fact, the similarity seen here is only in the outer region of the boundary layer in the case of a mesh away from the wall. Moreover, the increase in peak Reynolds stress values (figures 19 and 26*b*) and the strength of the vortex (figure 21*c*) with increasing y_m (and, equivalently, decreasing velocity ratio, $r = U_l/U_p = 0.84$–0.67) are in agreement with those reported by Wiecek & Mehta (1998) for plane mixing layers. Thus, the vortices downstream of the mesh seen along y_m in figures 15(*c*) and 16 possibly correspond to spanwise rollers (e.g. Bernal & Roshko 1986; Rogers & Moser 1992).

Control of streaks near the wall in FST-induced transition may not inhibit rapid recovery of streaks downstream, as the outer region of the boundary layer is less affected (Monokrousos *et al.* 2008). On the other hand, the present study suggests that, if the inclined high-shear layer or its lift-up and the associated structures are suppressed/distorted, transitional streaks fail to recover over a large downstream distance. Now, a grid/screen is used either to break large vortices (at the inlet of a

wind tunnel, for example) or in generating FST in many experimental studies. Here, disturbances from a mesh that is placed close to the wall are small, due to the small velocity gradient there, and are damped by viscosity. However, when it is away from the wall, disturbances from its bottom edge are large (figure 14*c*) and may enhance transition of the flow under mild acceleration; that is, mild in the sense that the flow is not under an accelerating free stream.

4. Summary and conclusion

An experimental study has been carried out to find the effect of flow modifications caused by a mesh placed normal to the flow and at different wall-normal locations, y_m, in the late stage of bypass transitions induced separately by an isolated cylindrical roughness element and a high level of FST on a flat plate. The mesh reduces the free-steam velocity by about 30 %, and causes a mild acceleration in the boundary layer. For the mesh away from the wall ($y_m \geqslant 4$ mm), the accelerated boundary layer velocity profiles exhibit overshoot, and the profile shape between the overshoot and the free stream is found to be of the plane mixing layer type.

When the mesh is placed close to the wall (at $y_m = 2$ or 4 mm), it causes transition delay over a large distance downstream of it. Transition delay in roughness-induced transition is mainly due to suppression of the lifted-up high-shear layer and disruption of the symmetric varicose type streaky structure, with eventual formation of orderly streaks (figures 5 and 10). Even in FST-induced transition, suppression of the lift-up of the high-shear layer (figure 15) seems to be the main cause for the transition delay reported here. As expected, the transition delay also reduces turbulence intensities, Reynolds stresses, turbulence production and boundary layer integral length scales like the displacement and momentum thicknesses. The number of clockwise vortices in the flow field also reduces.

With the mesh away from the wall, the lifted-up high-shear layer is not entirely suppressed even though boundary layer acceleration is present. Turbulence intensities in the boundary layer reduce over a short downstream distance from the mesh. However, disturbances generated by the bottom edge of the mesh increase the Reynolds stresses, turbulence production, number, size and strength of the anti-clockwise vortices in the outer region. These disturbances possibly enhance the transition of the mildly accelerated flow, leading to an increase in streamwise turbulence intensity far downstream of the mesh.

The large-scale streamwise structure in the wall-normal plane remains the same, except for a mild change in its size and inclination, for all mesh locations.

In conclusion, flow modification by suppression or distortion of the lifted-up high-shear layer and the associated spanwise structure in the late stage of transition can result in delaying transition over a large downstream distance. Although mild boundary layer acceleration and reduced Reynolds number (due to reduced free-stream velocity) together reduce the turbulence intensity, disturbances caused by the mesh in the outer region of the boundary layer may enhance transition. Finally, this study should be viewed as an important aspect of transition manipulation rather than a transition control strategy.

Acknowledgements

The authors sincerely thank the Department of Science and Technology for funding the PIV unit, under the FIST programme. Thanks are due to Professor V. Kumaran for lending us the laser unit. The comments and suggestions of the referees are gratefully acknowledged.

REFERENCES

ACARLAR, M. S. & SMITH, C. R. 1987 A study of hairpin vortices in a laminar boundary layer. Part 1. Hairpin vortices generated by a hemisphere protuberance. *J. Fluid Mech.* **175**, 1–41.

ADRIAN, R. J., CHRISTENSEN, K. T. & LIU, Z. C. 2000 Analysis and interpretation of instantaneous turbulent velocity fields. *Exp. Fluid* **29**, 275–290.

ASAI, M., MINAGAWA, M. & NISHIOKA, M. 2002 The instability and breakdown of a near-wall low-speed streak. *J. Fluid Mech.* **455**, 289–314.

BADE, K. & NAGUIB, A. 2012 Characteristics of a streak disturbance induced by an isolated roughness element. *Bull. Am. Phys. Soc. (In 65th Annual meeting of APS Division of Fluid Dynamics, San Diego, California)* **57** (17).

BAI, H. L., ZHOU, Y., ZHANG, W. G., XU, S. J., WANG, Y. & ANTONIA, R. A. 2014 Active control of a turbulent boundary layer based on local surface perturbation. *J. Fluid Mech.* **750**, 316–354.

BAKCHINOV, A. A., GREK, G. R., KLINGMANN, B. G. B. & KOZLOV, V. V. 1995 Transition experiments in a boundary layer with embedded streamwise vortices. *Phys. Fluids* **7**, 820–832.

BERNAL, L. P. & ROSHKO, A. 1986 Streamwise vortex structure in plane mixing layers. *J. Fluid Mech.* **170**, 499–525.

BERTOLOTTI, F. P. & KENDALL, J. M. 1997 Response of the Blasius boundary layer to controlled free-stream vortices of axial form. *AIAA Paper* 97–2018.

BI, C. -W., ZHAO, Y. P., DONG, G. H., XU, T. J. & GUI, F. K. 2014 Numerical simulation of the interaction between flow and flexible nets. *J. Fluids Struct.* **45**, 180–201.

BLACKWELDER, R. F. & KOVASZNAY, L. S. G. 1972 Large-scale motion of a turbulent boundary layer during relaminarization. *J. Fluid Mech.* **53**, 61–83.

BOIKO, A. V. 2001 Flat-plate boundary layer receptivity to a steady free-stream vortex disturbance. *Fluid Dyn.* **36** (6), 915–925.

BRANDT, L. 2007 Numerical studies of the instability and breakdown of a boundary-layer low-speed streak. *Eur. J. Mech. (*B*/Fluids)* **26**, 64–82.

BRANDT, L. 2014 The lift-up effect: the linear mechanism behind transition and turbulence in shear flows. *Eur. J. Mech. (*B*/Fluids)* **47**, 80–96.

BRANDT, L. & DE LANGE, H. C. 2008 Streak interactions and breakdown in boundary layer flows. *Phys. Fluids* **20**, 024107.

BRANDT, L., SCHLATTER, P. & HENNINGSON, D. S. 2004 Transition in boundary layers subject to free-stream turbulence. *J. Fluid Mech.* **517**, 167–198.

CHERNORAY, V. G., KOZLOV, V. V., LÖFDAHL, L. & CHUN, H. H. 2006 Visualization of sinusoidal and varicose instabilities of streaks in a boundary layer. *J. Vis.* **9**, 437–444.

CHOUDHARI, M. & FISCHER, P. 2005 Roughness-induced transient growth. In *35th AIAA Fluid Dynamics Conference and Exhibit, Toronto, Ontario Canada. AIAA Paper* 2005-4765.

CHRISTENSEN, K. T. & ADRIAN, R. J. 2001 Statistical evidence of hairpin vortex packets in wall turbulence. *J. Fluid Mech.* **431**, 433–443.

COSSU, C. & BRANDT, L. 2002 Stabilization of Tollmien–Schlichting waves by finite amplitude optimal streaks in the Blasius boundary layer. *Phys. Fluids* **14** (8), L57–L60.

DHAWAN, S. & NARASIMHA, R. 1957 Some properties of boundary layer flow during the transition from laminar to turbulent motion. *J. Fluid Mech.* **3**, 418–436.

DIXIT, S. A. & RAMESH, O. N. 2010 Large-scale structures in turbulent and reverse-transitional sink flow boundary layers. *J. Fluid Mech.* **649**, 233–273.

DURBIN, P. & WU, X. 2007 Transition beneath vortical disturbances. *Annu. Rev. Fluid Mech.* **39**, 107–128.

ELOFSSON, P. A., KAWAKAMI, M. & ALFREDSSON, P. H. 1999 Experiments on the stability of streamwise streaks in plane Poiseuille flow. *Phys. Fluids* **11**, 915–930.

FRANSSON, J. H. M., BRANDT, L., TALAMELLI, A. & COSSU, C. 2004 Experimental and theoretical investigation of the nonmodal growth of steady streaks in a flat plate boundary layer. *Phys. Fluids* **16**, 3627–3638.

FRANSSON, J. H. M., BRANDT, L., TALAMELLI, A. & COSSU, C. 2005 Experimental study of the stabilization of Tollmien–Schlichting waves by finite amplitude streaks. *Phys. Fluids* **17**, 054110.

FRANSSON, J. H. M., TALAMELLI, A., BRANDT, L. & COSSU, C. 2006 Delaying transition to turbulence by a passive mechanism. *Phys. Rev. Lett.* **96**, 064501.

GANAPATHISUBRAMANI, B., LONGMIRE, E. K. & MARUSIC, I. 2003 Characteristics of vortex packets in turbulent boundary layers. *J. Fluid Mech.* **478**, 35–46.

GUALA, M., HOMMEMA, S. E. & ADRIAN, R. J. 2006 Large-scale and very-large-scale motions in turbulent pipe flow. *J. Fluid Mech.* **554**, 521–542.

HACK, M. J. P. & ZAKI, T. A. 2014 Streak instabilities in boundary layers beneath free-stream turbulence. *J. Fluid Mech.* **741**, 280–315.

HANSON, R. E., BADE, K. M., BELSON, B. A., LAVOIE, P., NAGUIB, A. M. & ROWLEY, C. W. 2014 Feedback control of slowly-varying transient growth by an array of plasma actuators. *Phys. Fluids* **26**, 024102.

HE, G. S., PAN, C. & WANG, J. J. 2013 Dynamics of vortical structures in cylinder/wall interaction with moderate gap ratio. *J. Fluids Struct.* **43**, 100–109.

HERNON, D., WALSH, E. J. & MCELIGOT, M. 2007 Experimental investigation into the routes to bypass transition and the shear-sheltering phenomenon. *J. Fluid Mech.* **591**, 461–479.

HLADÍK, O., JONÁŠ, P. & URUBA, V. 2011 Dynamics of turbulent spots in transitional boundary layer. *J. Phys.: Conf. Ser.* **318**, 032028.

HONG, J., KATZ, J. & SCHULTZ, M. P. 2011 Near-wall turbulence statistics and flow structures over three-dimensional roughness in a turbulent channel flow. *J. Fluid Mech.* **667**, 1–37.

IMAYAMA, S., ALFREDSSON, P. H. & LINGWOOD, R. J. 2012 A new way to describe the transition characteristics of a rotating-disk boundary-layer flow. *Phys. Fluids* **24**, 031701.

JACOBS, R. G. & DURBIN, P. A. 2001 Simulations of bypass transition. *J. Fluid Mech.* **428**, 185–212.

KÄHLER, C. J. 2004 Investigation of the spatio-temporal flow structure in the buffer region of a turbulent boundary layer by means of a multiplane stereo PIV. *Exp. Fluids* **36**, 114–130.

KENDALL, J. M. 1998 Experiments on boundary-layer receptivity to freestream turbulence. *AIAA Paper* 98-0530.

KLEBANOFF, P. S., CLEVELAND, W. G. & TIDSTROM, K. D. 1992 On the evolution of a turbulent boundary layer induced by a three-dimensional roughness element. *J. Fluid Mech.* **237**, 101–187.

LANDAHL, M. T. 1980 A note on an algebraic instability of inviscid parallel shear flows. *J. Fluid Mech.* **98**, 243–251.

LITVINENKO, Y. A., CHERNORAĬ, V. G., KOZLOV, V. V., LOFDAHL, L., GREK, G. R. & CHUN, H. H. 2005 Nonlinear sinusoidal and varicose instability in a boundary layer. *Dokl. Phys.* **50**, 147–150.

LOUCKS, R. B. & WALLACE, J. M. 2012 Velocity and velocity gradient based properties of a turbulent plane mixing layer. *J. Fluid Mech.* **699**, 280–319.

LUCHINI, P. 2000 Reynolds-number-independent instability of the boundary layer over a flat surface: optimal perturbations. *J. Fluid Mech.* **404**, 289–309.

LUNDELL, F. 2007 Reactive control of transition induced by free-stream turbulence: an experimental demonstration. *J. Fluid Mech.* **585**, 41–71.

LUNDELL, F. & ALFREDSSON, P. H. 2003 Experiments on control of streamwise streaks. *Eur. J. Mech. (*B*/Fluids)* **22**, 279–290.

MANDAL, A. C. & DEY, J. 2011 An experimental study of boundary layer transition induced by a cylinder wake. *J. Fluid Mech.* **684**, 60–84.

MANDAL, A. C. & DEY, J. 2015 An experimental study on the generation and breakdown of boundary layer streaks. Manuscript is under preparation only.

MANDAL, A. C., VENKATAKRISHNAN, L. & DEY, J. 2010 A study on boundary-layer transition induced by free-stream turbulence. *J. Fluid Mech.* **660**, 114–146.

MANS, J., KADIJK, E. C., DE LANGE, H. C. & VAN STEENHOVEN, A. A. 2005 Breakdown in a boundary layer exposed to free-stream turbulence. *Exp. Fluids* **39**, 1071–1083.

MANU, K. V. 2013 Experiments on the late stages of boundary layer transition. PhD thesis, Department of Aerospace Engineering, Indian Institute of Science, Bangalore, India.

MANU, K. V., MATHEW, J. & DEY, J. 2010 Evolution of isolated streamwise vortices in the late stages of boundary layer transition. *Exp. Fluids* **48**, 431–440.

MATSUBARA, M. & ALFREDSSON, P. H. 2001 Disturbance growth in boundary layers subjected to free-stream turbulence. *J. Fluid Mech.* **430**, 149–168.

MONOKROUSOS, A., BRANDT, L., SCHLATTER, P. & HENNINGSON, D. S. 2008 DNS and LES of estimation and control of transition in boundary layers subject to free-stream turbulence. *Intl J. Heat Fluid Flow* **29**, 841–855.

NARASIMHA, R. & PRASAD, S. N. 1994 Leading edge shape for flat plate boundary layer studies. *Exp. Fluids* **17**, 358–360.

NARASIMHA, R. & SREENIVASAN, K. R. 1973 Relaminarization in highly accelerated turbulent boundary layers. *J. Fluid Mech.* **61**, 417–447.

NATRAJAN, V. K., WU, Y. & CHRISTENSEN, K. T. 2007 Spatial signatures of retrograde spanwise vortices in wall turbulence. *J. Fluid Mech.* **574**, 155–167.

NOLAN, K. 2009 On the measurement and analysis of turbulent spots evolving naturally due to freestream turbulence. PhD thesis, College of Engineering, University of Limerick, Ireland.

NOLAN, K. P. & WALSH, E. J. 2012 Particle image velocimetry measurements of a transitional boundary layer under free stream turbulence. *J. Fluid Mech.* **702**, 215–238.

NOLAN, K. P., WALSH, E. J. & MCELIGOT, D. M. 2010 Quadrant analysis of a transitional boundary layer subject to free-stream turbulence. *J. Fluid Mech.* **658**, 310–335.

NOLAN, K. P. & ZAKI, T. A. 2013 Conditional sampling of transitional boundary layers in pressure gradients. *J. Fluid Mech.* **728**, 306–339.

ORUÇ, V. 2012 Passive control of flow structures around a circular cylinder by using screen. *J. Fluids Struct.* **33**, 229–242.

OVCHINNIKOV, V., CHOUDHARI, M. M. & PIOMELLI, U. 2008 Numerical simulations of boundary-layer bypass transition due to high-amplitude free-stream turbulence. *J. Fluid Mech.* **613**, 135–169.

PATTEN, N., GRIFFIN, P. & YOUNG, T. M. 2013 Effects of freestream turbulence on the characteristics in the boundary layer near the transition onset location. *Trans. ASME J. Fluids Engng* **135**, 071203.

PIOMELLI, U., BALARAS, E. & PASCARELLI, A. 2000 Turbulent structures in accelerating boundary layers. *J. Turbul.* **1** (N1), 1–16.

RAHGOZAR, S. & MACIEL, Y. 2012 Statistical analysis of low- and high-speed large-scale structures in the outer region of an adverse pressure gradient turbulent boundary layer. *J. Turbul.* **13** (N46), 1–24.

ROGERS, M. M. & MOSER, R. D. 1992 The three-dimensional evolution of a plane mixing layer: the Kelvin–Helmholtz rollup. *J. Fluid Mech.* **243**, 183–226.

ROGERS, M. M. & MOSER, R. D. 1994 Direct simulation of a selfsimilar turbulent mixing layer. *Phys. Fluids* **6**, 903–923.

SCHLATTER, P., BRANDT, L., DE LANGE, H. C. & HENNINGSON, D. S. 2008 On streak breakdown in bypass transition. *Phys. Fluids* **20**, 101505.

SCHRADER, L.-U., BRANDT, L., MAVRIPLIS, C. & HENNINGSON, D. S. 2010 Receptivity to free-stream vorticity of flow past a flat plate with elliptic leading edge. *J. Fluid Mech.* **653**, 245–271.

SCHLATTER, P., DEUSEBIO, E., DE LANGE, R. & BRANDT, L. 2010 Numerical study of the stabilisation of boundary-layer disturbances by finite amplitude streaks. *Intl J. Flow Control* **2**, 259–288.

SHAHINFAR, S., FRANSSON, J. H. M., SATTARZADEH, S. S. & TALAMELLI, A. 2013 Scaling of streamwise boundary layer streaks and their ability to reduce skin-friction drag. *J. Fluid Mech.* **733**, 1–32.

SHAHINFAR, S., SATTARZADEH, S. S. & FRANSSON, J. H. M. 2014 Passive boundary layer control of oblique disturbances by finite-amplitude streaks. *J. Fluid Mech.* **749**, 1–36.

TANI, I., KOMODA, H., KOMATSU, Y. & IUCHI, M. 1962 Boundary-layer transition by isolated roughness. *Tech. Rep.* 375. Aeronautical Research Institute, University of Tokyo.

TOMKINS, C. D. & ADRIAN, R. J. 2003 Spanwise structure and scale growth in turbulent boundary layers. *J. Fluid Mech.* **490**, 37–74.

VOLINO, R. J., SCHULTZ, M. P. & FLACK, K. A. 2007 Turbulence structure in rough- and smooth-wall boundary layers. *J. Fluid Mech.* **592**, 263–293.

WALLACE, J. M., ECKELMANN, H. & BRODKEY, R. S. 1972 The wall region in turbulent shear flow. *J. Fluid Mech.* **54**, 39–48.

WANG, J. J., PAN, C. & ZHANG, P. F. 2009 On the instability and reproduction mechanism of a laminar streak. *J. Turbul.* **10** (N26), 1–27.

WESTIN, K. J. A., BOIKO, A. V., KLINGMANN, B. G. B., KOZLOV, V. V. & ALFREDSSON, P. H. 1994 Experiments in a boundary layer subjected to free stream turbulence. Part 1. Boundary layer structure and receptivity. *J. Fluid Mech.* **281**, 193–218.

WHITE, E. B. 2002 Transient growth of stationary disturbances in a flat plate boundary layer. *Phys. Fluids* **14**, 4429.

WIECEK, K. C. & MEHTA, R. D. 1998 Effects of velocity ratio on mixing layer three-dimensionality. *Exp. Therm. Fluid Sci.* **16**, 165–176.

WU, Y. & CHRISTENSEN, K. T. 2006 Population trends of spanwise vortices in wall turbulence. *J. Fluid Mech.* **568**, 55–76.

ZAKI, T. A. 2013 From streaks to spots and on to turbulence: exploring the dynamics of boundary layer transition. *Flow Turbul. Combust.* **91**, 451–473.

ZAKI, T. A. & DURBIN, P. A. 2005 Mode interaction and the bypass route to transition. *J. Fluid Mech.* **531**, 85–111.

ZHANG, C., PAN, C. & WANG, J. J. 2011 Evolution of vortex structure in boundary layer transition induced by roughness elements. *Exp. Fluids* **51**, 1343–1352.